

X-Ray Astronomy and Astrophysics

F.S. Porter, G.V. Brown, and J. Cottam

NASA/Goddard Space Flight Center, Greenbelt, MD 20771, USA
porter@milkyway.gsfc.nasa.gov

Abstract. The most compelling nature of X-ray astronomy is its richness and scale. Almost every observable object in the sky either naturally emits X-ray radiation or can be probed by X-ray absorption. Current X-ray observatories such as *Chandra* and *XMM-Newton* have considerably advanced our understanding of many of these systems by using dispersed X-ray spectrometers and imaging CCD cameras. However, it is the combination of these two techniques, a true broad-band, high spectral resolution, imaging spectrometer, that will drive the next revolution in X-ray astronomy. This is where Low Temperature Detectors can play a key role but also where the science will continuously challenge the technology. In this Chapter we will explore the constraints that both the science goals and the space environment place on the implementation of LTDs, and the solutions implemented in current missions such as the XQC and the XRS on *Astro-E2*. In addition we will see how the *NeXT*, *Constellation-X*, and *XEUS* missions will drive LTD instruments to a much larger scale. Finally, we will address scaling rules in current LTD detectors and where the LTD community needs to proceed to address both the science goals and expectations of the astrophysics community.

1 The Wealth and Breadth of the X-Ray Universe

X-rays are emitted by high-energy phenomena throughout the observable universe from the shock heating in stellar winds and supernova remnants, to the accretion processes in binary systems or in the nuclei of active galaxies, to the virialization of matter in intracluster gas. X-rays provide an excellent probe of the energetics and physical conditions in nearly all classes of astrophysical objects; the direct emission from these sources or the reprocessed spectra as the light interacts with the material along the line of sight are highly diagnostic and contain detailed spectroscopic signatures of the emitting and absorbing plasmas. Analysis of these spectra provides quantitative information on the physical conditions in these plasmas and ultimately allow us to study the physics of these different phenomena.

Over the past forty years since the first discovery of extra-solar X-ray sources [1], the field of X-ray astronomy has progressed rapidly. From the early 1960s to the late 1970s, X-ray detectors consisted primarily of proportional counters. The increasing sensitivity of these missions led to the detection of hundreds of X-ray sources. Although proportional counters are

very efficient photon counters, they have poor energy resolution. Other than the detection of a few bright spectral features, including the Fe K fluorescence line, spectroscopy was limited to basic comparisons between the global shapes of the spectra. Significant progress was made in the late 1970s and early 1980s when focusing optics became available. This led to orders of magnitude increase in sensitivity and hence in the number of detected X-ray sources. With focusing optics, dispersive spectrometers could be implemented, which provided several orders of magnitude increase in the spectral resolution. Unfortunately, the collecting area of these instruments was low, which limited their use to only the brightest sources. In the 1990s solid-state imaging spectrometers were launched with sufficient sensitivity to catalogue tens of thousands of sources from nearly all classes of astrophysical objects. Solid state imaging detectors also provided a significant improvement in spectral resolution over proportional counters. Discrete emission and absorption features with sufficient contrast could be identified, and basic imaging spectroscopy could be performed. However, because the resolving power of these instruments was only moderate, spectroscopic analysis required fitting often degenerate spectral models to the unresolved spectral features.

In the past few years, X-ray instruments have finally become available with sufficiently high throughput and spectral resolution to allow for quantitative X-ray spectroscopy of extra-solar objects. The first to fly are the diffraction grating spectrometers on-board NASA's *Chandra* X-ray Observatory [2] and ESA's *XMM-Newton* Observatory [3]. These spectrometers have revolutionized the field of X-ray astrophysics. Because they are dispersive spectrometers, they are excellent for point sources with soft X-ray spectra, but the spectral resolution degrades both with increasing energy and with increasing source extent. Cryogenic spectrometers, such as the XRS microcalorimeter that will shortly be launched as part of the joint NASA and ISAS/JAXA *Astro-E2* observatory, have resolving powers that increase with energy and that are independent of source extent. These instruments are critical to the progress of X-ray astrophysics. Not only will they fill the current need for high-resolution spectroscopy at high energies, but, as the technology develops, low-temperature detectors have the potential to finally provide true broad-band, high-resolution imaging spectroscopy of all types of sources.

In this chapter we will briefly discuss the X-ray spectroscopy that motivates the development of LTD detectors and the strengths of LTD detectors in the context of current spectroscopic instruments. We will then describe the development and use of current LTD instruments and the challenges of future missions.

2 High-Resolution X-Ray Spectroscopy

An X-ray spectrum from an astrophysical object provides excellent quantitative information about the emitting source and any absorbing plasmas

along the line of sight. The flux in a given emission line depends on the microphysical conditions in the plasma, such as the temperature and electron density, that determine the fraction of ions in each excited state, the rates of excitation and de-excitation, and the energy level populations. The shape, observed energy, and orbital phase-dependence of the spectral line depend on global properties such as the velocity distribution and geometry of the plasma. Quantitative analysis of the discrete spectral features can therefore be used to measure and map the conditions in these plasmas. In this section we will describe some of the spectroscopic diagnostics relevant to X-ray sources and the instrument resolving powers necessary to access them.

2.1 Ionization Mechanism

One of the most basic spectroscopic questions is the mechanism by which the plasma is ionized. The coronae of stars, the shocked gas of old supernova remnants, and even intracluster gas are collisionally ionized. The ions are mechanically heated by direct interactions with the surrounding free electrons, and they cool radiatively through bremsstrahlung emission, recombination, and line emission. The spectrum of a plasma in collisional ionization equilibrium (CIE) is essentially determined by the temperature of the plasma, which dictates the strengths of the line emission through the rates of excitation and recombination. The temperature of a CIE plasma is comparable to the ionization potential for observed ions. X-ray emission can therefore be observed from collisionally ionized plasmas with temperatures of $0.1 \leq k_B T \leq 10$ keV. A second method of ionization is photoionization where the material is ionized by the absorption of photons from an external radiation field, and it cools by radiative recombination and electron cascade. The circumstellar material in accretion-powered binaries, stellar winds, and the clouds around active galactic nuclei are examples of photoionized plasmas. For a plasma in photoionization equilibrium (PIE) the emitted spectrum depends both on the plasma temperature and on the shape and intensity of the ionizing source, which determines the rates of ionization. PIE plasmas are characterized by the ionization parameter, $\xi = L_x/n_e r^2$, where L_x is the luminosity of the ionizing source, n_e is the electron density, and r is the radial distance to the ionizing source. Since a PIE plasma is highly over-ionized relative to a CIE plasma of the same local electron temperature, X-rays can be observed from photoionized plasmas with much lower temperatures. Excellent reviews of the physics of collisionally ionized and photoionized plasmas can be found in *Mewe* [4] and *Liedahl* [5] respectively.

There are many spectroscopic differences between collisionally ionized and photoionized plasmas, and it is fairly straightforward to distinguish them (Fig. 1). The simplest diagnostic is the presence of radiative recombination continua (RRC) features. When electrons with a Maxwellian distribution recombine onto an ion, photons with energies of $\chi + k_B T$ are emitted, where χ is the ionization potential. In photoionized plasmas the temperatures are

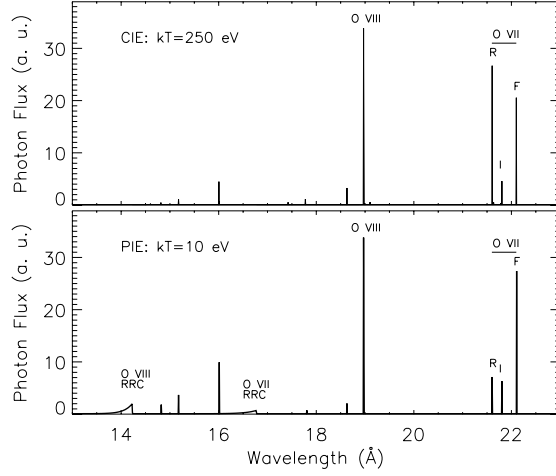


Fig. 1. Simulated oxygen emission spectra for a collisionally ionized plasma (*top*) and a photoionized plasma (*bottom*). The ratio of the O VII He-like lines and the presence or absence of RRC features are simple diagnostics of the ionization mechanism

lower than the ionization potential so the emitted photons, or RRC features, appear as narrow cusp-like features in the spectrum. In collisionally ionized plasmas, where the temperature is comparable to the ionization parameter, the RRC are too wide to be distinguished from the continuum emission.

Another simple diagnostic is the ratio of lines emitted by He-like ions, the resonance line, the intercombination lines, and the forbidden line. In a collisionally ionized plasma, where the energy levels are populated by direct excitation followed by cascade, the resonance line dominates the observed He-like emission. In a photoionized plasma, where the energy levels are populated by recombination and cascade from higher energy levels, the triplets are preferentially populated. The observed ratio of these lines, $G = (i + f)/r$, can be used to distinguish between a collisionally ionized and a photoionized plasma [6].

2.2 Temperature Structure

There are multiple spectral diagnostics that can be used to measure the temperature of a plasma. A simple diagnostic in photoionized plasmas comes from the RRCs. The widths of these features is a direct measure of the plasma temperature as $\Delta E \sim k_B T$. For collisionally ionized plasmas, the rate of ionization and the rate of recombination both depend on the temperature of the plasma. The ionization balance is therefore a unique function of the plasma temperature. In a photoionized plasma, the rate of ionization depends instead on the incident photon spectrum so the ionization balance is a more

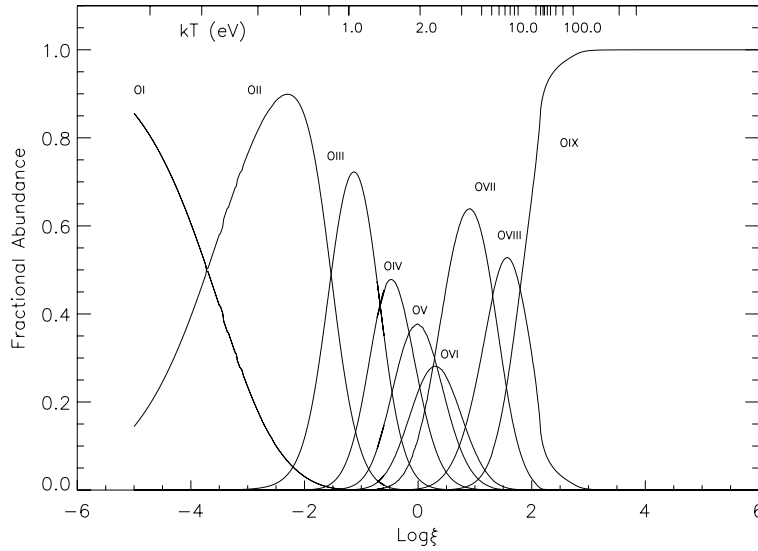


Fig. 2. Ionization balance for oxygen in a photoionized plasma ($\Gamma = 2$) where $\xi = L_x/n_e r^2$ is the ionization parameter. The relationship between the ionization parameter and the plasma temperature has been calculated using the XSTAR program [7]

complicated function. Figure 2 shows the ionization balance for oxygen in a photoionized plasma. The dependence on both temperature and ionization parameter are shown. This diagnostic is especially useful with sources like the cooling flows in clusters of galaxies where iron emission features can be detected from a range of ionization states. Measuring the observed line ratios for the different ions provides an excellent measure of the plasma temperature independent of the elemental abundances.

2.3 Density Structure

The ratio of lines in the He-like series depends additionally on the electron density. At sufficiently high electron densities, electron-ion collisions will excite electrons in the upper level of the forbidden transition to the upper level of the intercombination transitions as the rate of excitation becomes comparable to the rate of radiative decay. The line intensity of the intercombination features relative to the forbidden features, $R = i/f$, can therefore provide a measure of the electron density [6]. This is illustrated in Fig. 3. For most abundant elements (C, N, O, Ne, Mg, Si, S, and Fe) the critical densities are in the range of $n_e = 10^8 - 10^{14} \text{ cm}^{-3}$. Unfortunately, UV photons can also photo-excite the same transitions. If the UV flux at the excitation energy is sufficiently high it will compete with or mask the density effects. This can be

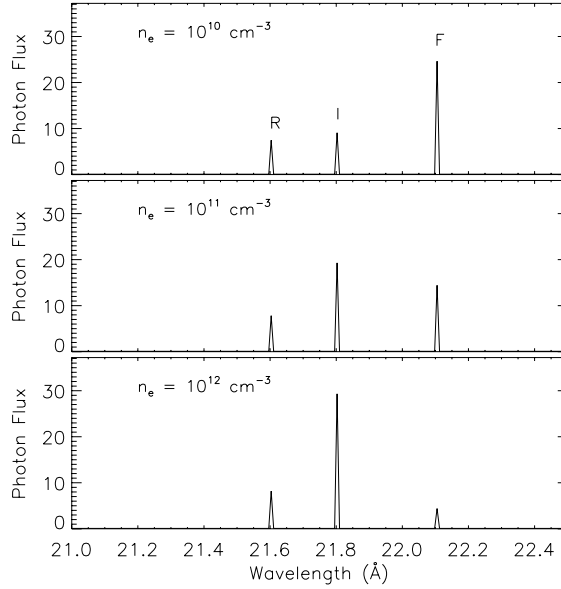


Fig. 3. Density diagnostics for the Oxygen He-like series in a $k_B T = 10$ eV photoionized plasma. The two intercombination lines are not resolved at the resolution of the figure

the case in binary star systems where the photoionized winds from a massive star are illuminated by UV emission.

2.4 Velocity Structure

The velocity structure in the absorbing or emitting plasma will affect the shape and centroid of the spectral features. Bulk motion along the line of sight will Doppler-shift the line centroid by $\Delta E/E_0 = v/c$, where E_0 is the nominal energy of the line transition and v is the velocity of the material. Velocity fields within the plasma produce features that appear broadened due to the integrated projected velocity distributions. The line shape is therefore a measure of the velocity fields.

2.5 Optical Depth

Material along the line of sight will attenuate the X-ray emission and generate discrete spectral features that are sensitive to the temperature, density and thickness of the absorbing material. The continuum absorption is described by $F = F_0 e^{-\tau}$, where F_0 is the initial flux and τ is the optical depth. The optical depth for a given ion, is described by $\tau = n_i \sigma d$ where n_i is the ion density, σ is the scattering cross section, and d is the distance traversed. The scattering cross section, σ , decreases with increasing energy as

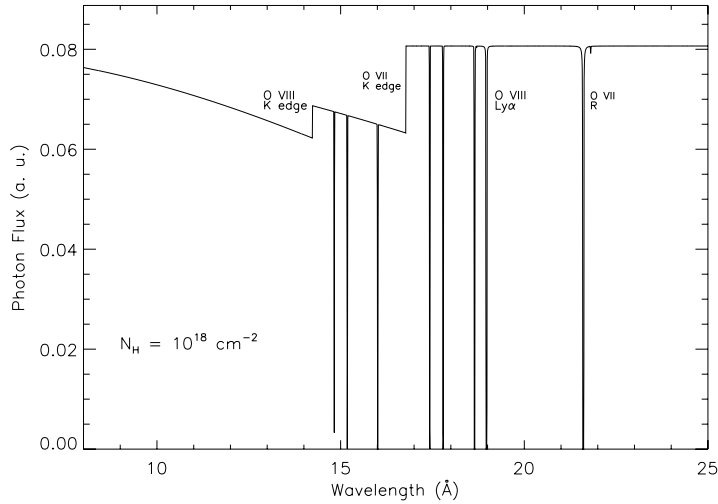


Fig. 4. A simplified absorption spectrum of oxygen. The absorption edges as well as the discrete absorption lines are visible

$\sigma(E) \sim \sigma(\chi)(E/\chi)^{-3}$ to produce the familiar edge feature in the continuum spectrum. The cross sections for discrete transitions are orders of magnitude larger than for continuum scattering. Discrete absorption features can therefore be used to probe material with a wide range of optical depths. A simplified absorption spectrum of oxygen is shown in Fig. 4. A plasma with thermal or turbulent velocities will absorb photons with a range of energies around the transition energy to produce absorption features that are broadened as $\Delta E/E = \sqrt{(2k_B T/m_e c^2)}$ for thermal broadening and $\Delta E/E = v_{\text{turb}}/c$ for turbulent broadening. Absorption spectroscopy is clearly extremely useful in characterizing astrophysical plasmas from the near-neutral material in the interstellar medium to the highly-ionized molecular clouds around active galactic nuclei.

2.6 Fluorescence Emission

When an inner-shell electron is ionized, the excited ion will stabilize through radiative decay, which is called fluorescence, or by ejecting an upper-level electron, which is called the Auger effect. The rate of decay by fluorescence emission depends on the energy of the transition and therefore scales with the atomic number as Z^4 . The rate of Auger emission depends on the Coulomb interaction between the electrons and is therefore independent of atomic number. The fluorescence yield, which is the efficiency of fluorescence relative to Auger emission, is therefore low for all abundant elements except iron. Since iron is found in almost all types of astrophysical objects, iron fluorescence spectroscopy is an important diagnostic.

Fluorescence can occur in neutral to highly-ionized ions, so emission lines can be seen from material over a range of temperatures and ionization parameters. The ionization balance in the fluorescence emission can be used to determine the temperature structure in the emitting material. In practice, this is complicated by the fact that in near-neutral ions the inner-shell energy levels are not significantly affected by the screening of the outer electrons. The individual lines can therefore be difficult to distinguish. For example, Fe K α fluorescence emission lines from Fe I, to Fe XV are all within $\sim 1 \times 10^{-3} \text{ \AA}$ of $\lambda = 1.940 \text{ \AA}$ [8]. Emission lines from more highly ionized iron are more easily separable.

2.7 Instrument Requirements

The resolving powers of the instruments limit which spectral diagnostics are accessible. At the most basic level, resolving the charge states of an element in order to measure the ionization balance requires separating the strongest lines, typically those of the H-like and He-like ions. The spacing between these lines scales with the atomic number roughly as $\Delta E \sim 10Z$ and the line energies scale as $E \sim 10Z^2$ [9] so a resolving power of $\mathcal{R} = E/\Delta E \geq Z$ is required to separate these features. Measuring the plasma density requires separating the intercombination lines from the forbidden line in the He-like ions. The energy separation between these lines scales as $\Delta E \sim 0.3Z^{4/3}$ [9] so resolving powers of $\mathcal{R} \geq 14(Z-1)$ are required. Measuring the width of an RRC in order to determine the temperature of a photoionized plasma requires a resolving power of $\mathcal{R} \geq \chi/k_{\text{B}}T$. Measuring Doppler shifts requires resolving powers of $\mathcal{R} \geq c/v$ while measuring velocity widths requires resolving powers of $\mathcal{R} \geq \sqrt{2}c/v$. The resolving powers required for these spectroscopic diagnostics are summarized in Fig. 5. An excellent review of spectroscopic diagnostics, and the required instrumental resolving powers is given in *Paerels* [10]. In designing new spectrometers, or evaluating the usefulness of possible instrumentation, these resolution requirements must be taken into account.

3 Instrumentation for X-Ray Spectroscopy

X-ray spectrometers can be divided into two general categories, dispersive and non-dispersive. Dispersive spectrometers exploit the wave properties of light; they measure the wavelength of photons by deflection as they interact with discrete, periodic structures such as crystals or diffraction gratings. Non-dispersive spectrometers exploit the particle nature of photons; they convert photons into electrons, as in the case of proportional counters or charge coupled devices (CCDs), or into heat, as in the case of microcalorimeters. Dispersive and non-dispersive spectrometers have different strengths and limitations. Historically, non-dispersive spectrometers have been flown because of their efficiency, but their resolving powers are low. The recently launched

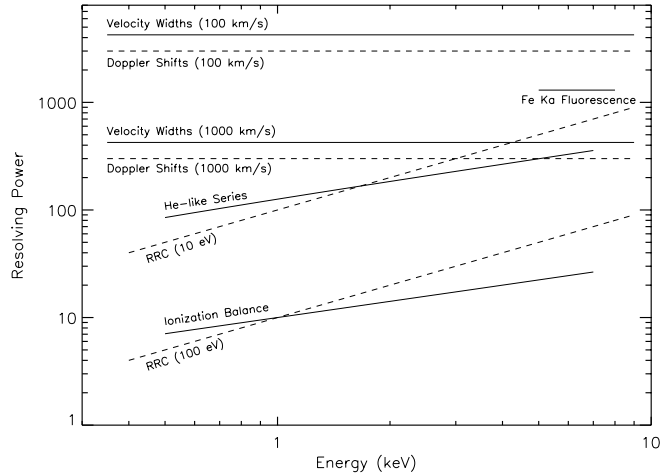


Fig. 5. Resolving power as a function of energy for the spectroscopic diagnostics described in Sect. 2

high-resolution instruments on both the *Chandra* and *XMM-Newton* observatories are dispersive spectrometers. Low temperature detectors offer the possibility of high-resolution in a non-dispersive spectrometer. In this section we will discuss these different types of instruments and describe the current applications of each.

3.1 Dispersive Spectrometers

Dispersive spectrometers operate on the principle of diffraction. The resolving power depends directly on the magnitude of the dispersion, which in turn depends on the spacing of the dispersive elements. In crystal spectrometers these elements are the lattice spacing of the crystals. In diffraction grating spectrometers the dispersive elements are the periodic grooves that are manufactured on or through a grating. Dispersive spectrometers require a narrow incident beam, since the angular width of the incident beam determines the blur in the dispersed beam that degrades the resolution of the instrument. Any spatial extent in the X-ray source also decreases the instrument resolving power. For most dispersive spectrometers, the resolution is nearly constant in wavelength. The resolving power therefore increases with increasing wavelength or decreasing energy. Dispersive spectrometers are optimal for soft X-ray point sources. Past high-resolution spectrometers have mostly employed transmission gratings and crystal spectrometers. These were successfully flown on the *EXOSAT* and *Einstein* Observatories [11, 12]. Transmission gratings are also used for the high-resolution spectrometers on-board *Chandra*. The *XMM-Newton* high-resolution spectrometer uses reflection gratings.

These two new high-resolution spectrometer are described in more detail below.

3.1.1 Chandra

The *Chandra* Observatory was launched in July 1999. It carries a high angular resolution telescope designed for arcsecond X-ray imaging. Two rings of transmission gratings are mounted on hinges that can be alternately rotated into the optical path behind the telescopes to create the High-Energy Transmission Grating Spectrometer (HETGS) [13] and the Low-Energy Transmission Grating Spectrometer (LETGS) [14]. These gratings intercept the focused X-ray beam and diffract the photons according to the equation, $m\lambda = d(\sin \theta - \sin \chi)$ where m is the spectral order, d is the grating line spacing, and θ and χ are the incident and diffraction angles relative to the grating normal. The dispersed light is imaged at the focal plane by either the Advanced CCD Imaging Spectrometer (ACIS [15]) or the High Resolution Camera microchannel plate (HRC [16]). The intrinsic energy resolution of these focal plane detectors is used to separate the spatially overlapping spectral orders. The HETGS is composed of two types of grating elements, the High Energy Grating (HEG) and the Medium Energy Grating (MEG) that are spatially offset to form a shallow ‘X’ on the focal plane. The HEG has a wavelength resolution of $\Delta\lambda_{\text{FWHM}} \sim 0.012 \text{ \AA}$. It is optimized for the 1.2–15 Å band. The Medium Energy Grating (MEG) has a wavelength resolution of $\Delta\lambda_{\text{FWHM}} \sim 0.023 \text{ \AA}$. It extends the HETGS coverage to $\sim 30 \text{ \AA}$. The LETGS contains more widely spaced grating elements with a wavelength resolution of $\Delta\lambda_{\text{FWHM}} \sim 0.05 \text{ \AA}$. It is designed to cover the 1.2–175 Å wavelength band. The resolving power and the effective area of these instruments is shown in Fig. 6. The *Chandra* grating spectrometers provide extraordinary spectral resolution for bright point sources in the soft X-ray band. Spatially extended sources with angular extents of $\Delta\theta = 1$ arcs degrade the instrument resolving power by a factor of ~ 3 .

3.1.2 XMM-Newton

The *XMM-Newton* observatory, launched in December 1999, contains the Reflection Grating Spectrometer (RGS) [17], a high resolution dispersive spectrometer. The telescopes on the *XMM-Newton* are optimized for throughput and not angular resolution. The wide angular resolution ($\Delta\theta \sim 15$ arcs) of the *XMM-Newton* precludes the use of transmission gratings. Instead, the high-resolution RGS spectrometer employs reflection gratings. These disperse light according to $m\lambda = d(\cos \beta - \cos \alpha)$, where α and β are the incident and dispersion angles with respect to the grating surface. For a telescope with an intrinsic angular resolution of $\Delta\alpha$, the grating resolving power is $\mathcal{R} = (\cos \beta - \cos \alpha)/(\sin \alpha \Delta\alpha)$. By going to grazing angles, the resolving

powers can be made large. There are two RGSs on-board the spacecraft. In each an array of 180 reflection gratings is permanently mounted to intercept the focused light emerging from the telescope mirrors. The gratings intercept approximately half the emerging light and disperse it onto offset arrays of CCDs. The remaining photons pass through the empty spaces in the grating arrays onto the European Photon Imaging Camera (EPIC [18]) for simultaneous broad-band imaging spectroscopy. The RGS has a wavelength resolution of $\Delta\lambda_{\text{FWHM}} \sim 0.06 \text{ \AA}$ over the wavelength band of 5–35 Å. The properties of the RGS are shown in Fig. 6. The RGS provides high collecting areas and high resolving powers in the soft X-ray band making it ideal for studying lower flux sources. Because the resolving power depends less on the width of the telescope beam, sources with small spatial extents ($\Delta\alpha \leq 0.5 \text{ arcmin}$) can still be studied without a significant reduction in the spectral resolution.

3.2 Non-Dispersive Spectrometers

Dispersive spectrometers have revolutionized the spectroscopy of point sources such as stars, X-ray binaries, and many active galactic nuclei, but high-resolution spectroscopy of most extended sources, such as supernova remnants and clusters of galaxies, and of high-energy spectral features has been very difficult. The HETGS spectrometer on *Chandra* covers the high energy band to 10 keV, but the resolving power degrades to $\mathcal{R} \sim 100$ making quantitative spectroscopy difficult at high energies. The RGS on *XMM-Newton* has been used to measure spectral parameters of moderately extended sources. However using current dispersive spectrometers for extended sources is problematic at best and requires complex global modeling. Non-dispersive spectrometers are needed to obtain unambiguous diagnostic information for both extended sources and the high energy band above 2 keV.

Non-dispersive spectrometers operate by absorbing individual photons and converting their energy into recordable quantities, such as electrons or heat. The simplest non-dispersive spectrometers are gas-filled proportional counters. Incident photons ionize the absorbing gas, and cause cascades of electrons. The total number of freed electrons is proportional to the energy of the incident photon as $N = E/W$, where W , the work function, is equal to the ionization energy of the gas, typically $\sim 30 \text{ eV}$. This electron signal is then amplified, either by electronic bias or by gas scintillation and then read out as a pulse. The energy resolution of proportional counters depends on the statistical fluctuations in the number of electrons as well as the properties of the amplifying avalanche. The limit of a traditional proportional counter is $\mathcal{R} \sim E^{1/2}$. Gas scintillation proportional counters have 2 to 3 times better resolving powers because of the scintillation signal amplification. Proportional counters are the “work horses” of X-ray astronomy. They have flown repeatedly in X-ray missions beginning with the earliest extra-solar X-ray detector [1], through to currently orbiting observatories such as the Proportional Counter Array (PCA) on the *Rossi X-ray Timing Experiment (RXTE)* [19].

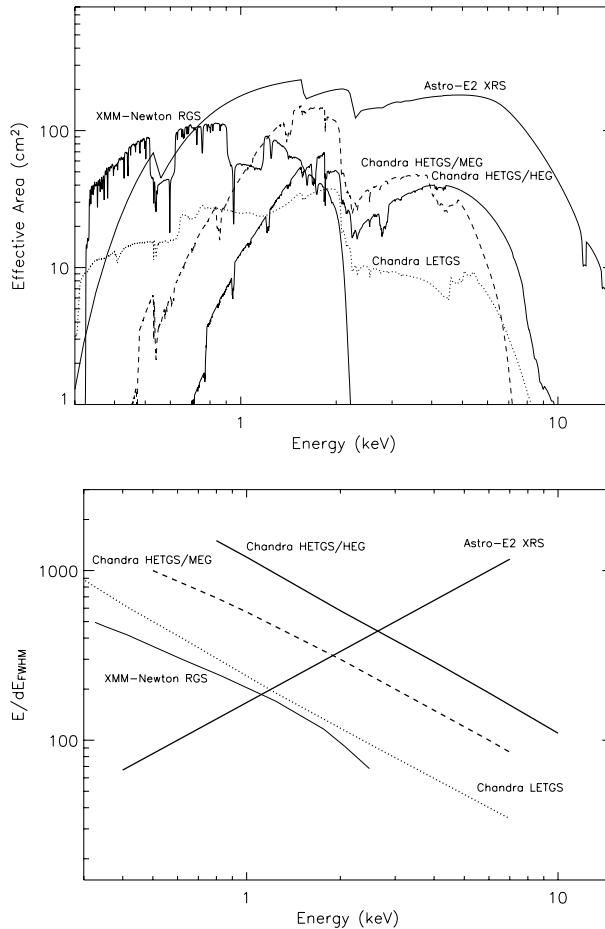


Fig. 6. The resolving power and effective area of the high-resolution spectrometers on-board the *Chandra*, *XMM-Newton*, and the *Astro-E2* Observatories. The values are plotted for the standard configurations of each instrument, and spectral order $m = \pm 1$ for the *Chandra* gratings and $m = -1$ for the *XMM-Newton* gratings

The development of solid-state spectrometers, and particularly charge coupled devices (CCDs) has significantly advanced non-dispersive spectroscopy. A CCD consists of a doped semiconducting material, usually silicon. When a photon is absorbed, freed electrons jump from the valance to the conduction band. The band gap for a solid state device is typically ~ 3 eV so many more electrons are freed than in a proportional counter. A gate structure traps the ionized charge in localized “pixels” until it is electrically transferred off the silicon chip in a serial electronic readout. The energy resolution of a CCD is much higher than a proportional counter because of the smaller work function, the large charge collection and transfer efficiency, and

the development of low noise readout electronics. CCDs can have resolving powers of up to $\mathcal{R} \sim 50$. Although the spectral resolution is much lower than that of current dispersive spectrometers, the pixelation of CCDs (typically $\sim 24 \mu\text{m}$) allows them to be used for imaging spectroscopy. X-ray CCDs were first flown on *ASCA* [20]. The *ASCA* detectors provided spectral imaging of a wide range of objects with sufficient resolution to uniquely identify bright emission and absorption features. X-ray CCDs are currently used on the *Chandra* X-ray Observatory as the Advanced CCD Imaging Spectrometer (ACIS [15]) and on the *XMM-Newton* Observatory as the European Photon Imaging Cameras (EPIC [18, 21]). X-ray CCDs have provided extraordinary X-ray images of the sky and within the limits of the spectral resolution, compelling imaging spectroscopy.

Since the energy resolution of non-dispersive spectrometers is roughly constant or increasing with energy, the resolving powers increase with increasing energy. The energy resolution is independent of source size making them ideal for studying spatially extended sources. However, in spite of these properties, the best CCD spectrometers still cannot compete with the spectral resolution of dispersive spectrometers.

3.3 The Niche for Low Temperature Detectors

Low temperature detectors (LTDs) have the potential to provide both high-resolution spectroscopy and imaging capabilities in the same instrument. An LTD array is intrinsically an imaging device, since the location of the X-ray in the focal plane is uniquely determined. Resolving powers of $\mathcal{R} \sim 500$ to 2000 have been demonstrated over a broad energy band of 1 to 10 keV. An LTD is therefore a spatial-spectral imaging detector where every pixel in the focal plane array gives a complete high-resolution spectrum of the source. LTD instruments are non-dispersive. As such they provide resolving powers that are independent of the angular extent of the source. LTDs can therefore observe spatially extended objects with the same spectral resolution as point sources.

LTDs have additional benefits. Since they are not integrating detectors, they convey precise timing information for each photon, with high “pile-up” limits. LTDs can therefore be used for precision spectroscopy of rapidly varying sources such as X-ray binaries. LTDs are also broad-band spectrometers. They can be tuned to cover almost any spectral range from optical to gamma-ray energies with some tradeoff in the resolving power as the energy band is expanded. Most X-ray LTDs easily cover the full band from 0.1 to 10 keV with a single instrument. Finally, LTDs are very efficient photon detectors. The quantum efficiency is limited at energies below 1 keV by the infra-red blocking filters, and at the high energy end by the absorption cross sections of the absorbing material. However, across most of the 0.1 to 10 keV band the quantum efficiency is near unity.

Ultimately, LTDs are inherently complementary to the existing X-ray spectrometers. The energy resolution of the HETGS on *Chandra* is $\Delta E_{\text{FWHM}} = 0.6 \text{ eV}$ at the He-like oxygen lines. This is an order of magnitude better than most LTDs at the same energy. The EPIC/MOS CCDs on *XMM-Newton* have 2.5 megapixels, each with spectral resolving power of $\mathcal{R} \sim 50$. LTDs are at least a decade away from achieving arrays of this scale. Although they cannot compete in either of these regions of phase space, LTDs uniquely offer high resolving powers at energies above 2 keV and the possibility for simultaneous high-resolution imaging spectroscopy of all types of astrophysical sources regardless of spatial extent. An ideal observatory would contain a full complement of instruments: a large field of view CCD imager, a high resolution dispersive spectrometer covering the region below 1 keV, and an LTD instrument with broad dynamic range, high resolving power, and precision timing. In fact most future X-ray observatories, including *Astro-E2*, *NeXT*, *XEUS* and *Constellation-X* will employ a mix of these instruments. As the next sections will describe, LTDs have a great deal to offer future X-ray observatories.

4 Ground Rules for Low Temperature Detectors in X-Ray Astronomy

X-ray astronomy fundamentally requires space-based instruments since the earth's atmosphere is opaque to all but the highest energy X-rays. While high altitude balloons allow access to X-rays with energies in excess of 20 keV, the rest of the X-ray band (0.1–10 keV) is completely inaccessible below about 100 km altitude. The lower energy band below 10 keV contains all the emission lines from the abundant astrophysical elements, and thus many of the diagnostic spectral features that motivate X-ray observations. X-ray observatories must therefore operate in space.

The ground rules for making LTDs usable for X-ray astronomy constrain how the instrument must be packaged for an orbiting observatory or sub-orbital rocket. This generally means that the instruments need to be compact, low-power and stable against launch vibration. The instrument must also be robust for long term operation in a space environment. The spaceflight requirements for LTD instruments affect everything from the cryogenic cooling to the room temperature electronics. In this section we will review these restrictions, how they affect the design of X-ray LTD instruments, and some of the methods used to overcome these obstacles.

4.1 Cryogenics

Most non-dispersive, high-resolution, X-ray detector systems, including microcalorimeters based on silicon, transition-edge, and magnetic thermistors,

operate at relatively low temperatures, usually below 0.1 K. Cryogenic systems on satellites have a long history and are typically complex, bulky, and expensive. The need for a sophisticated system to cool below 0.1 K drives a large part of the size and cost of an X-ray LTD instrument.

4.1.1 Adiabatic Demagnetization Refrigerators

Temperatures below 0.1 K have been readily achieved on the ground for almost 80 years, first using Adiabatic Demagnetization Refrigerators (ADRs) and then with closed-cycle systems, such as dilution refrigerators. In addition, it has been possible for over 40 years to commercially purchase ADRs and dilution refrigerators for laboratory use. Starting in the mid-1960s, large commercial dilution refrigerators supplanted the adiabatic demagnetization refrigerator with the widespread availability of ^3He . This is largely due to the much higher cooling capacity, continuous operation, and lower base temperatures that can be achieved with a dilution refrigerator. The move to space-borne instruments, however, limits the cooling options to what can be achieved in a fully-automated, zero-gravity, low-power system. The standard ^3He recirculating dilution refrigerator with its large pumps and gas handling systems, and its reliance on gravity to maintain the phase separated region in the mixing chamber, is a poor match for spaceflight. Although substantial progress has been made in adapting the dilution refrigerator for space [22], all current and planned cryogenic X-ray missions use an ADR as the lowest temperature stage.

An ADR is basically an entropy pump and operates by cycling in the S , T (entropy, temperature) plane using an external magnetic field applied to a dilute spin system. The spin system can be made very dilute by using a heavily hydrated paramagnetic salt such as Ferric Ammonium Alum (FAA, $\text{FeNH}_4(\text{SO}_4)_2 \cdot 12\text{H}_2\text{O}$). For FAA the entire magnetic moment of the molecule is in the 4d unpaired electron in the single iron atom. The rest of the material, including the 12 waters of hydration, simply serves to keep the dipoles far apart, suppressing the ordering temperature to below 30 mK and making it useful for magnetic cooling. A good introduction to ADRs can be found in *Lounasmaa* [23] and ADRs for spaceflight in *Serlemitsos et al.* [24].

The original ADRs used from the 1930s to the mid 1960s used bulky external water cooled magnets to cool very small magnetic samples suspended on silk threads in glass cryostats. At about the same time that ADRs were being replaced in the laboratory with dilution refrigerators, the key to modern and spaceflight ADRs, the compact, high-field superconducting magnet, was also becoming widely available. An ADR with a superconducting magnet turns out to be an excellent match for space cryogenic detectors; it requires no gas recirculation, no gravity, and is a fully solid-state system with no moving parts. It does, however, require a high current magnet and, in some cases, as in TES or magnetic microcalorimeters, a large amount of magnetic shielding. Unfortunately, the ADR, especially in a single stage design, also has

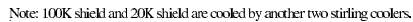
relatively low cooling power, typically a few microwatts, so careful cryogenic design is required. The first spaceflight ADRs have already been produced for the XQC and XRS instruments that are described in Sect. 6.

4.1.2 Cryogenics, Cryo-coolers, and Lifetime

In addition to the complex low temperature refrigerator, lifetime is the single biggest hurdle for cryogenic X-ray instruments in space. ADRs require a precooling stage as low as 1K to remove the cyclical heat of magnetization, to minimize radiative heating, and to intercept conductive heat on the ADR suspension system and wiring layer. The current X-ray LTD instruments use liquid cryogenics as the precooling stage. The cryogen lifetime is limited, however, by the thermal conductance of the dewar structure, wiring, and dissipation due to the ADR and the detector system. Orbiting instruments generally must be launched with their entire stock of cryogenics. When the cryogenics are exhausted, the instrument ceases to function. Thus the lifetime of the instrument is limited by the mass and volume allocation for the instrument on the observatory. For reasonable lifetimes of a year or more, the instruments tend to be bulky and dominate the mass and volume budgets of the observatory.

One way of achieving a relatively long lifetime is to simply launch a large quantity of liquid helium. This was the approach used on *COBE* which included a massive 660 liter superfluid helium cryostat with a lifetime of about 10 months. Clearly, scaling the *COBE* system for a multi-year lifetime quickly becomes intractable. Another method is to use a fully closed-cycle mechanical refrigeration system such as that planned for *Constellation-X*. The lifetime of a mechanical system is only limited by the robustness of the mechanical cooler, and not by the consumption of any stored resource. Between these two extremes there is a large phase space for hybrid systems, such as that employed by the XRS instrument on *Astro-E2*. The XRS uses a three stage precooling system for the ADR including a cryo-cooler, a 120 liter solid neon cryogen tank, and a 32 l superfluid helium cryogen tank. A multistage cryogenic system allows for a much smaller cryostat than the *COBE* system for a longer lifetime.

Multi-stage cryogenic systems can give a long instrument lifetime. The XRS instrument, for example, achieves a lifetime of over three years on only 32 l of helium. However, at over 400 kg, the instrument dominates the *Astro-E2* spacecraft. This limits our ability to form partnerships on small-scale missions. In order to reduce the instrument's footprint we must minimize the use of heavy cryogenics and move to cryogen-free, mechanical cooler based cryostats. The baseline for most future missions is a cryogen free design using some combination of mechanical cryo-coolers (Stirling, pulse-tube, etc...), sorption coolers, Joule-Thomson coolers, He-3 sorption coolers, and finally a one or more stage ADR. The exact mix of these components varies from mission to mission, and none of the instrument designs has yet been frozen.



only limited by the robustness of the coolers [28]

As an example, a preliminary cryogen-free design for the *NeXT* X-ray observatory is shown in Fig. 7. The design space for cryogenic systems thus seems large but there are also large constraints including the maturity of the technologies. Ultimately, a cryogen free, low power, low mass design is required if LTDs are to move from highly specialized, one-of-a-kind instruments that dominate a spacecraft to a ubiquitous system that is a ready choice for multi-instrument spacecraft. X-ray LTDs would then be an option not only for X-ray astronomy, but also for space plasma physics, and even possibly X-ray microanalysis instruments on future planetary landers.

4.2 Mass and Power

A spaceflight cryogenic X-ray instrument has serious mass and power constraints. For example, the M-V launch vehicle for the *Astro-E2* spacecraft has a launch capability of about 1800 kg to low earth orbit. The XRS instrument, not including its electronics and focusing optics, weighs over 400 kg. In comparison, the Pegasus launch vehicle used in NASA's small-explorer (SMEX) program, has a capability of about 400 kg into a 475 km circular orbit. Clearly LTD instruments are tightly mass constrained, and at least in their current form, incompatible with some launch opportunities.

The power budget of the spacecraft is similarly constrained. Spacecraft power is limited of course by the size of the solar panels, but also the significant mass of the batteries that operate the spacecraft when the sun is eclipsed. For example, the *Astro-E2* observatory has a total power budget of about 660 W for a power system that weighs a total of 147 kg. On a large multi-experiment observatory, an LTD instrument can only consume a small fraction of the available resources. The XRS instrument, for example, uses a total average power of 64 W and a peak power of 120 W during operation.

Large reductions in mass are possible but usually result in substantial increases in instrument power for cryogenic systems. The move to fully cryo-cooler based designs substantially increases the power consumption of the cryogenic instrument and also requires the addition of a radiator to dump the waste heat from the instrument. These added complexities, however, substantially shrink the mass of the instrument. The addition of the cryo-cooler to the XRS instrument consumes 35 W but lengthens the hold time of the solid Ne by 50%, a potential mass savings of 85 kg of Ne, not including the additional mass of the cryostat structure. The added mass of the XRS cooler is only 4.2 kg. Hybrid designs for a proposed SMEX X-ray mission have achieved predicted lifetimes of 2 years in less than 110 kg using a hybrid pulse-tube cooler/Ne/He/ADR design. *Constellation-X*, *XEUS*, and *NeXT* plan to go yet further, with totally cryogen-free designs. The *Constellation-X* requirement is for at least a 5 yr lifetime in under 100 kg with no consumables.

The cost for all of this savings in mass is power and efficiency. The cryo-coolers do not achieve even close to Carnot efficiency and this magnifies the problem. The efficiency of a Carnot cycle refrigerator is

$$\eta = \frac{T_1}{T_2 - T_1}, \quad (1)$$

where T_1 is the base temperature and T_2 is the higher reject temperature. Real systems achieve far less. The small (4.2 kg) *Astro-E2* cryo-cooler manufactured by Sumitomo Heavy Industries achieves about 8% of Carnot efficiency, giving 1 W of cooling power down to 80 K for a 35 W input. The lower temperature coolers planned for future missions do even worse. One design for *NeXT* would have 5 mW at 1.7 K for 180 W input giving about 0.5% of Carnot. Note, however that the 5 mW is about a factor of five more cooling

power than on the *Astro-E2* helium tank and with a lifetime only limited by the robustness of the cooler. The 1.7 K cooler for *NeXT* has the additional advantage of only requiring a very simple single stage ADR. In this case one can trade power against the complexity of the lowest temperature stage. The *Constellation-X* baseline design includes only a 6 K lowest temperature cryo-cooler stage requiring a complex 5 stage ADR and a custom high-temperature magnet system.

Finally, cryogenic X-ray detectors have relatively power-hungry electronics. Unlike integrating detectors, cryogenic X-ray instruments must process the entire X-ray pulse time-series, one event at a time. In addition, to achieve the highest resolution we must use a matched (optimal) filter. The optimal filter gives a 40% increase in the resolving power over using a shaping amplifier and a peak-hold-sample system such as is often used in nuclear instrumentation [25]. However, in order to calculate and then apply the optimal filter, one must process the entire X-ray event waveform using on-board processing. This requires fast digitizers, fast digital signal processors (DSPs), and a fair amount of on-board memory. On the XRS, the digital pulse processing electronics consumes about 25 W of peak power for 32 detector channels using a discrete DSP for each channel. Obviously this sort of system does not scale well to very large arrays.

4.3 Survivability: Mechanical Design and Analysis, Radiation Damage

A key requirement for space-based detector systems is, of course, survivability. The instruments must be tested and qualified to the maximum vibration loads expected during launch. The XRS on *Astro-E2* was tested to static loads of 25 g axial, and 9 g lateral, and random loads of 9 g_{rms} axial and 3 g_{rms} lateral. Sounding rocket experiments are tested to random vibration levels of 13 g_{rms} and must, in addition, contend with the landing shocks of up to 200 g. This puts a heavy structural burden on cryogenic detector systems which must also require a great deal of internal thermal isolation.

Clearly, the spaceflight environment severely affects the design space for LTD instruments. The soft, cantilevered suspension systems that are adequate for laboratory cryostats are not acceptable for spaceflight. The instrument must be designed with careful staging of the resonant frequencies in the cryostat so that vibration on the outer shell of the instrument does not pump energy into high-Q resonances on the inner parts of the instrument including the detector system. For example, the XQC sounding rocket instrument sits on vibration isolation mounts that attach it to the rocket shell with a resonant frequency of about 30 Hz. The re-entrant shell He tank suspension has a resonant frequency of 130 Hz, and the tensioned ADR+detector system has a resonant frequency of 450 Hz [26]. This staged-resonance system results in a factor of almost 1000 isolation of the detector stage from rocket vibrations.

In addition, the detectors themselves have to be designed with resonant frequencies staged yet higher than the detector heat sink, typically in excess of 1 kHz. This is not a trivial task because the pixel suspension for microcalorimeters must also provide their thermal isolation. For XRS, the detector heat sink has a resonant frequency of about 350 Hz. The XRS detectors were then designed to have their first resonant mode at over 2 kHz [27]. As an added complication, the detector suspension has to be designed so that the static stress from differential thermal contraction is well below the yield strength of the materials.

The staged resonances necessary for survivability during launch also must serve to isolate the detector system from microphonic noise from spacecraft systems such as momentum wheels, and cryo-coolers. In the laboratory, detector systems are isolated from environmental vibration using soft damping systems. This becomes much more difficult on a spacecraft since soft damping systems would have to be locked during launch. In addition, a soft damping system would have to be carefully designed to avoid alignment errors with the X-ray focusing optics. Thus, space-borne detector systems must rely almost exclusively on the staged resonance system for isolation from microphonic interference to the detector signal.

Radiation damage is also a significant problem in space. The environment in near earth orbit is somewhat protected by the earth's magnetosphere, but the particle background is still considerable. Once beyond the magnetosphere, such as the 2nd Lagrange point (L2) orbit planned for *Constellation-X*, the observatory will receive the full force of the solar wind. Small-gate electronic components are heavily susceptible to damage from particle interactions. This limits the choice of components that are usable for an LTD instrument. The fast modern processors that one might use in the laboratory for event processing, are almost certainly not available in a radiation-hard version suitable for spaceflight. In addition, detector system components such as SQUIDs and the detectors themselves must be tested for radiation damage including long term effects such as activation. A full radiation analysis is usually required for a spaceflight instrument including radiation testing of all components. This issue must be confronted during the development of the detector system and not solely when it is adapted for spaceflight.

4.4 Electronics

The electronic readout and analysis systems for LTD instruments are also heavily constrained in space. The electronics for LTD instruments typically consist of a cryogenic amplifier, a room temperature amplifier, a digital event processing system, an ADR controller, and possibly a cryo-cooler controller. As we have discussed these must conform to the mass and power constraints for a spaceborne observatory. In addition, low telemetry rates mean almost all event processing must occur on the spacecraft. All the electronics necessary

for an LTD instrument must be small, low power, and have low data rates commensurate with the finite telemetry bandwidth on a satellite observatory.

The electronic readout system for cryogenic detectors can vary considerably from field effect transistor (FET) front end amplifiers for silicon microcalorimeters, to superconducting quantum interference device (SQUID) readout of TES and magnetic microcalorimeters, to tuned oscillators for RF kinetic inductor detectors. There are, however, several commonalities that affect the system design. Once beyond the analog amplification, the digital processing is nearly identical.

The key building blocks for an LTD readout system include:

1. Wiring layer from the detectors to the first stage amplifiers and between the first stage amplifier and any additional cryogenic amplification stages.
2. Cryogenic amplification stages.
3. Cryogenic multiplexer electronics and/or bandpass filters for frequency division multiplexing.
4. Wiring layer to room temperature and staged heat sinks to minimize thermal conduction.
5. Room temperature analog electronics which include additional amplification, and control and feedback electronics for the cryogenic amplifiers.
6. Digital electronics which includes pulse reconstruction from the multiplexer (phase sensitive detection or time reconstruction), triggering, optimal filter generation and application, and event grading.
7. ADR temperature controller, including temperature diagnostics for the whole instrument.
8. Cryo-cooler controller.

There are also a large number of housekeeping functions that must be handled by the on-board electronics including temperature monitoring, noise characterization, detector and cryogenic amplifier diagnostics, and logic to handle off-nominal situations such as keeping the telemetry stream from saturating.

The XRS, for example, performs these tasks with separate analog and digital electronics boxes with a discrete amplifier and pulse processing chain for each pixel. Scaling to 1000+ channels, however, requires a completely different architecture. The wire count from the low temperature amplifiers, and to some extent, the room temperature analog electronics can benefit substantially from using cryogenic multiplexers. One design for *Constellation-X* uses time division multiplexing to read out 32 columns of 32 detectors, reading out the 32 rows in parallel and sampling the 32 columns in a round-robin fashion. This requires controlling and feeding back to only 32 SQUID amplifier chains at a time, growing the room temperature amplifier chain only as the number of Rows N rather than the number of channels N^2 . The digital electronics, however, benefits from no such scaling.

In a multiplexed design, the digital electronics must, in addition to all of the pulse processing, perform the reconstruction necessary to separate the

multiplexed channels from each other. The digital electronics must reconstruct the data stream time series *per channel* in order to process the event stream. Unfortunately one cannot use a dedicated DSP for each channel as in the XRS because of both power and mass constraints.

A simple scaling of the XRS digital electronics from 32 to 1000 channels brings the peak power requirements to almost 1000 W. This is not possible for a space-borne observatory that may have a total power budget significantly less than this. There are additional issues of size, mass, and the 1000 W of waste heat. A solution is to move the event triggering to specialized logic that *precedes* the event processing. The triggering logic would be responsible for breaking the time series for each channel into an event stream with a channel tag that is then assigned to a free processor in a processor farm. The power for the pulse processing then scales with the *event rate* rather than the *number of channels*. Preliminary designs for *Constellation-X* have shown that it is possible to process 10^4 events/s in less than 80 W using 8 processors. When the event rate is low, some of the processors can even be put in a lower power state to further reduce the average power.

Scaling to 1000 channels appears to be an achievable task, especially using a cryogenic multiplexing scheme and a pulse-processing farm at room temperature. A 1000 channel detector system appears possible *in principle* but has not yet been achieved, and there are certainly significant design challenges left to be overcome. Even with these improvements the readout electronics for cryogenic detectors do not scale well making very large detector arrays extremely difficult.

4.5 Risk

Lastly we discuss some of the practical rather than technical constraints of using cryogenic detectors in space. Cryogenic detectors and their infrastructure are new and largely untested on space platforms. This is changing, especially with the launch of XRS in mid 2005. However, one must justify the *risk* of using unproven technology and the expense of its full development cost to traditionally conservative technical review panels in order to win approval for new missions. Risk, in the management definition, includes anything that can interfere with the success of the mission from an outright failure of the observatory, launch vehicle, or ground support equipment, to delayed development cycles, and overspent budgets.

In today's risk averse environment proposing new technology can be difficult. Demonstrating low risk must involve full system modeling for both short term instrument survivability as well as the long term viability in space, including effects such as radiation damage. Winning approval for new space instruments requires that these systems issues are addressed up-front, with viable full instrument designs, analysis, and demonstrations. This is at least as important as demonstrating the ultimate performance of the detector system itself. In a head-to-head competition, a low-risk proposal will almost

always win over an instrument with slightly higher performance but also higher perceived risk.

5 Current and Near-Term Missions

After almost two decades of development, X-ray LTD instruments are finally becoming a reality. Two such instruments have already been completed, the X-ray Quantum Calorimeter (XQC) sounding rocket, and the X-ray Spectrometer (XRS) on the US-Japanese *Astro-E2* observatory. In addition, there are several ambitious, large-scale observatories, *NeXT*, *Constellation-X*, and *XEUS*, that are currently in the planning stages. All of these missions include an X-ray LTD focal plane instrument.

In this section we describe, in detail, the XQC and XRS instruments as the first generation of X-ray LTD instruments. This includes some of the design parameters and challenges in implementing a cryogenic detector system for spaceflight. In the last section, we briefly discuss the three nearest term LTD missions. The requirements of the next generation missions provide huge challenges for the LTD community. Our success at designing and deploying kilopixel arrays for these new missions will govern whether and how low temperature X-ray detectors are carried into the future.

5.1 The X-Ray Quantum Calorimeter: The First LTD X-Ray Mission

5.1.1 Introduction to the XQC

The X-ray Quantum Calorimeter (XQC), a collaboration between the University of Wisconsin and NASA's Goddard Space Flight Center, is the first space-borne cryogenic X-ray instrument. It had its maiden flight in December, 1995 and has flown a total of three times on a sub-orbital sounding rocket achieving an altitude of 240 km and a total flight time of about 15 min. Its primary purpose is to study the soft diffuse X-ray emission in the band from 0.03–1 keV with high spectral resolution. The large spatial extent and low surface brightness of the emission makes this a task uniquely suited to an LTD instrument.

The soft, diffuse X-ray background, first observed by proportional-counter based sounding rockets in the 1960's, is the brightest X-ray object in the sky [29, 30]. The emitting source is currently believed to be a superposition of a number of physical processes including: thermal emission in the galactic halo, thermal emission in a region of nearby diffuse gas in the "local bubble", charge exchange between the solar wind and geocoronal gas, charge exchange between the solar wind and the interstellar medium, and, thermal emission from the intergalactic medium. However, this is largely supposition since the individual components cannot be uniquely separated using the otherwise

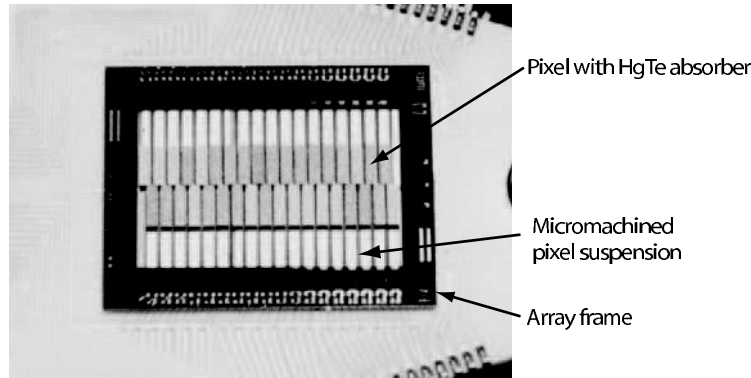


Fig. 8. The XQC 2×18 microcalorimeter array

exquisite spatial maps compiled by the University of Wisconsin all sky survey [31] and the *ROSAT* all sky survey [32]. Detailed spectroscopy is required in order to break the degeneracy between the various emission mechanisms, to look, for example, for the specific spectral signature for thermal emission as opposed to charge exchange. A good review of the soft X-ray background can be found in *McCammon* and *Sanders* [33].

Although the Diffuse X-ray Spectrometer (DXS) instrument observed regions of the soft X-ray background in the low energy band from 0.15 to 0.284 keV with high resolution ($\Delta E = 5\text{--}17\text{ eV}$), the results were difficult to interpret. This band includes the crowded L-shell emission from many abundant elements including Si, S, Mg, and Ar. Higher resolution is required to deconvolve the blended lines. The XQC experiment is designed to look at the larger spectral band from 0.03 to 1 keV. This contains the much less crowded 0.75 keV spectral band that includes the emission from O VII, O VIII, Ne IX and L-shell Fe as well as the Fe IX, X, XI emission around 70 eV. The XQC is designed to answer fundamental questions on the origin of the soft X-ray background, including the emission mechanism(s) and the composition and state of the emitting material.

5.1.2 The XQC Instrument

The XQC is launched on a Nike-Black Brant two stage sounding rocket. This is a short duration suborbital flight giving about 5 min of observing time above 100 km altitude where the atmosphere is thin enough for acceptable X-ray transmission in the low energy band. To acquire reasonable statistics in such a short flight, the XQC has a field of view that covers a full steradian on the sky. There is no spatial information other than the 1 sterad aperture stop. The observation is purely spectroscopic. A full description of the instrument can be found in *McCammon* et al. [34] and *Porter* et al. [35].

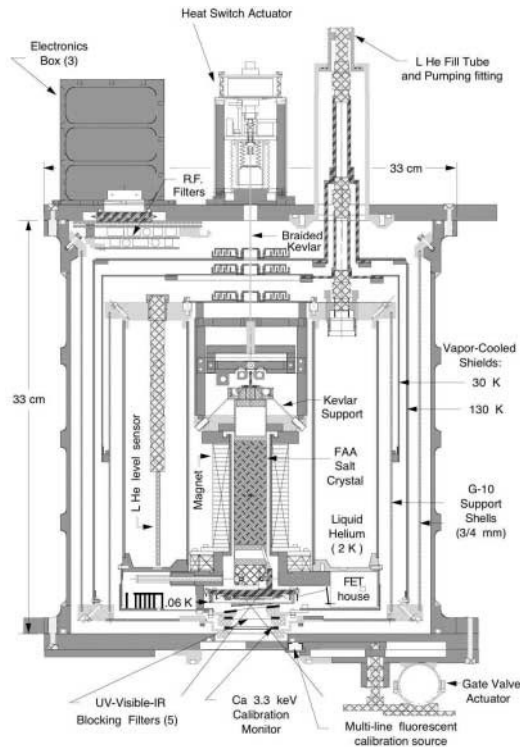


Fig. 9. A cross section of the X-ray Quantum Calorimeter (XQC) cryostat showing the helium tank, vapor cooled shields, ADR, and analog electronics. Reprinted from [34]

The XQC detector system is optimized for the largest possible detector area, with a high quantum efficiency only up to 1 keV. The detector consists of a 36 channel 2×18 “bilinear” array of microcalorimeter detectors with doped silicon thermistors as shown in Fig. 8. These are large-area pixels compared to most X-ray microcalorimeter instruments, with 1 mm^2 per pixel. The X-ray absorber is HgTe, a compromise material with a high quantum efficiency, a moderate Debye temperature of about 140 K, and most importantly, a high thermalization efficiency. Since the bandpass of the XQC only extends up to 1 keV, the absorber material is made very thin, around $0.7 \mu\text{m}$, deposited by molecular chemical vapor deposition (MoCVD) onto a silicon backing layer. This configuration minimizes the heat capacity of the absorber while supporting the thin absorber material. The absorbers are then epoxied onto silicon spacer blocks attached to the micro-machined, implanted silicon detector array.

The XQC contains all of the sub-systems needed for a long term cryogenic X-ray mission, in miniature form including a small 4 l liquid helium dewar

and a 50 g FAA salt pill in its adiabatic demagnetization refrigerator. The cryostat, shown in cross section in Fig. 9, is a two stage cryogenic system with a pumped volume of ^4He at 1.6 K and a single stage Ferric Ammonium Alum (FAA) ADR [34]. The XQC uses a 50 g salt pill in a 40 kG NbTi superconducting magnet. The total heat load at the 60 mK operating temperature from radiation, wiring, and the Kevlar suspension system is below $1\text{ }\mu\text{W}$ giving a hold time for the refrigerator of about 12 h on the ground. The four liter liquid helium bath is a single cryogen system with vapor cooled shields and a total parasitic heat load of 98 mW giving a 24 h hold time below 1.6 K. Since the flight time is only 15 minutes this is adequate for both pre-flight testing and for the heat input into the system during launch. The ADR is cycled on the ground about two hours before launch and holds at 60 mK (open loop during launch) until it lands on its parachute at the end of the flight. The XQC was and is a great success in demonstrating the key technologies required for cryogenic X-ray instruments in space.

The XQC electronics do not perform high-resolution pulse processing on the spacecraft. The detector electronics have hardware pulse triggering electronics, and telemeters down the entire waveform for each X-ray pulse for subsequent processing on the ground. This is possible because the XQC includes two 800 kb continuous telemetry channels allowing the X-ray event waveforms to be downlinked in real time. The system also includes a “quick look” system consisting of a shaping amplifier, a peak and hold system, and an ADC to give low resolution (between 15 and 20 eV FWHM) real time spectral information during the flight.

On the ground, the telemetry is received in real time. This allows in-flight monitoring of the quick-look spectral information and over 200 telemetered engineering parameters. Post-flight, the data is then optimally filtered, gain-drift corrected, and an energy scale added to produce an in-flight spectrum. Cosmic ray interactions in the detector are also filtered out to reduce the background signal. Figure 10 shows the final calibration spectrum taken on the ground, immediately preceding a launch in 1999. The preflight spectrum was integrated for 9000 seconds up to 4 minutes before launch with the instrument on the launch rail using an internal ^{244}Cm alpha fluoresced multi-target X-ray source that produces a number of calibration lines below 1 keV. A ^{41}Ca internal conversion X-ray source also continuously illuminates the array with 3.3 and 3.6 keV potassium K X-rays on the ground and during flight for gain-drift monitoring.

5.1.3 XQC Results and Future Plans

The XQC has flown three times since 1995. The most recent flight in March of 1999 yielded a high quality spectrum of a 1 sterad field of view centered on $l = 90^\circ$, $b = +60^\circ$ in galactic coordinates. This is a bright area in the soft X-ray sky near the north galactic pole that is otherwise devoid of bright, soft X-ray emitting objects. The instrument had a composite resolution of

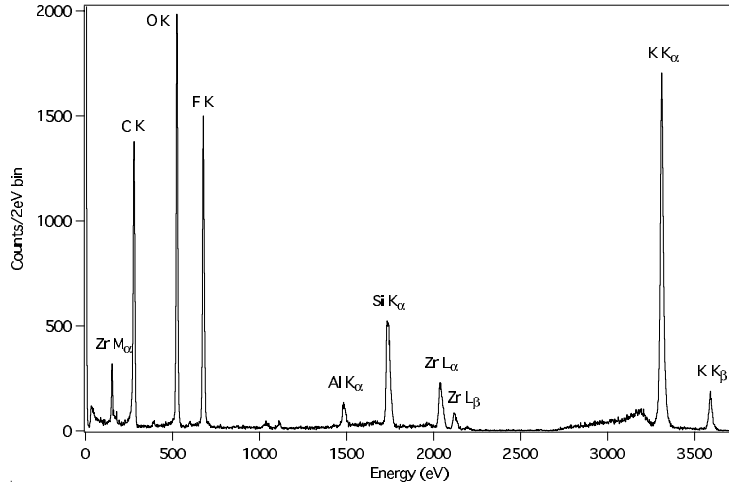


Fig. 10. XQC preflight calibration spectrum. The spectrum was integrated for 9000 s up to 4 min before launch with the instrument on the launch rail at White Sands Missile Range. Calibration sources were a ^{244}Cm alpha fluoresced multi-target source and a ^{41}Ca internal conversion source

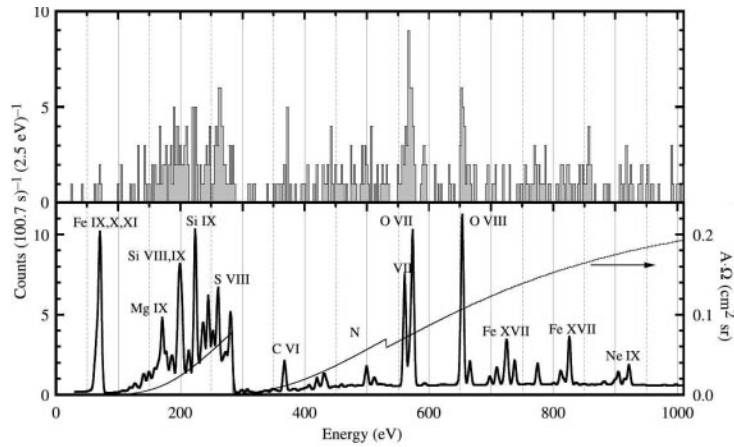


Fig. 11. (Top) Spectrum of the soft X-ray sky observed with the XQC instrument in March, 1999. (Bottom) A standard two component thermal model for the soft X-ray background folded through the XQC response function. The XQC throughput function is shown on the bottom panel, right hand axis. Reprinted from McCammon et al. [34]

$\sim 9\text{ eV}$ across its spectral band. The in-flight spectrum is shown in Fig. 11. Emission lines from O VII, O VIII and C VI are clearly detected. A complete discussion of the results and their implications is contained in [34].

The XQC experiment is limited by the collecting area, even with a 1 sterad field of view. In addition, the 1 sterad field of view washes out the spatial detail shown in the UW and *ROSAT* all sky maps. The collecting area of the array needs to be increased to improve the statistics and to reduce the aperture to increase the spatial information. Higher spectral resolution is also needed, for example, to resolve the He-like oxygen K emission lines, and to look for the emission lines from Fe L-shell transitions which should be present in a 0.3 keV thermal plasma, even if the abundance of iron is largely depleted. The next rocket flight will consist of 4 mm² pixels, in a 6×6 36 pixel array using the “deep implant” process used successfully for the XRS program. Operating at 50 mK a spectral resolution of less than 4 eV at $E = 1$ keV is expected with four times the collecting area of the current XQC experiment.

The long term solution is to fly a soft X-ray cryogenic detector system on an orbiting platform and to perform an all sky survey with high spectral resolution. In addition to resolving the local components of the soft X-ray background, an observatory of this type could observe the spatial distribution of the hot intergalactic medium which has important implications for cosmology. This has been proposed several times for NASA’s small and medium explorer program and has received high ratings for both the science and the technology readiness but has not yet been selected for flight.

5.2 The XRS on Astro-E2

5.2.1 Introduction to the XRS

The X-Ray Spectrometer (XRS) is a long term U.S.–Japanese collaboration to put a high-resolution, broad-band, non-dispersive X-ray spectrometer at the disposal of the astrophysics community. The instrument is part of the *Astro-E2* X-ray observatory to be launched in early 2005 on a Japanese M–V launch vehicle. The observatory, in addition to the XRS, contains four wide field CCD cameras, the X-ray Imaging Spectrometer (XIS), with a total of 800 cm² collecting area at 1 keV, and the Hard X-ray Detector (HXD) [36], with a bandpass from 10 keV to over 600 keV. Together this observatory will have both spectroscopy and imaging capabilities covering a very large dynamic range from 0.1 keV to 600 keV. The XRS provides high-resolution spectroscopy, the CCD cameras provide wide field imaging, and the HXD provides spectral information to very high energies. The observing program includes both a guaranteed time program and a large guest investigator program for the X-ray astrophysics community from 2005 to at least 2008 when the cryogens of the XRS are exhausted. The observatory will observe every major class of X-ray emitting object including supernova remnants, stellar coronae, active galaxies, galaxy clusters, X-ray binaries, comets, and the interstellar medium in our own and neighboring galaxies. The XRS instrument is the flagship instrument on the *Astro-E2* spacecraft and represents a culmination of the state-of-the-art in cryogenic X-ray instrumentation.

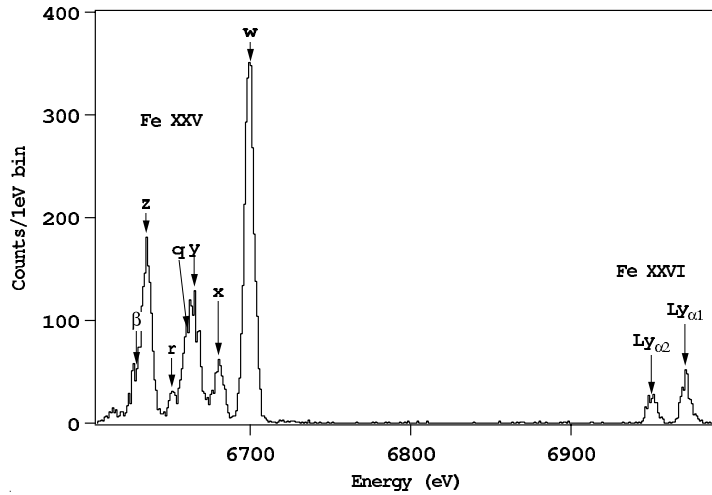


Fig. 12. X-ray spectrum of highly ionized He-like Fe XXV and H-like Fe XXVI taken with a laboratory XRS microcalorimeter array at the EBIT-I facility at Lawrence Livermore National Laboratory

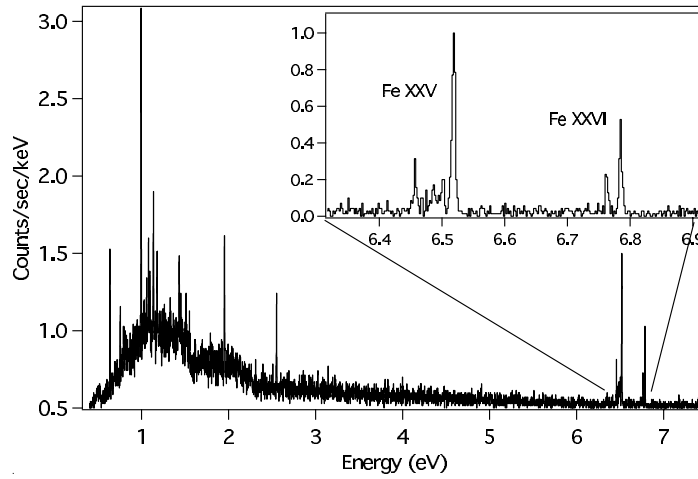


Fig. 13. A simulated X-ray spectrum of the Ophiucus cluster of galaxies using the X-ray Spectrometer (XRS) on the *Astro-E2* observatory. The simulation is for a 35 ks observation of the X-ray emitting cluster plasma with a temperature of 11.6×10^6 K. Compare the *inset* to Fig. 12 that shows an actual XRS spectrum of highly ionized iron in the laboratory

The XRS complements the high resolution dispersive instruments on *Chandra* and *XMM-Newton*. The XRS has higher spectral resolution and more effective area above 2 keV than the RGS on *XMM-Newton* and the HETG on *Chandra* (see Fig. 6), and because it is non-dispersive its spectral resolution is not affected by the angular extent of the object. The XRS will observe extended sources such as supernova remnants and galaxy clusters, without degradation and without heroic tomographic measurements. The higher spectral resolution of the XRS above 2 keV makes the XRS uniquely suited for studying the K-shell emission from iron which is a crucial diagnostic for the study of X-ray emitting objects because it has a high abundance, a high fluorescent yield, and emits in a relatively uncrowded area of the X-ray spectrum. The XRS has the spectral resolution to largely deconvolve the He-like Fe XXV line emission, whose line ratios give an important temperature and density diagnostic of the emitting medium. The XRS can also separate the H-like Fe XXVI Ly $_{\alpha}$ lines from the neighboring dielectronic recombination lines giving another important temperature diagnostic. As an example, Fig. 12 shows a spectrum of Fe XXV and XXVI produced in the laboratory using the EBIT-I electron beam ion trap. The spectrum was taken with a laboratory XRS instrument with a microcalorimeter array identical to the flight array. For comparison, a simulation of the predicted Fe K emission from a cluster of galaxies using the XRS flight instrument is shown in Fig. 13.

5.2.2 The XRS Cryogenic System

Figure 14 shows the completed XRS instrument prior to installation on the *Astro-E2* spacecraft. The XRS is the first X-ray LTD system designed for long term operation in space. As such, the design of the XRS conforms to all of the ground rules discussed in Sect. 4 and all future instruments will build on this experience. Here we review some of the characteristics of the XRS.

The XRS instrument is a four stage cryogenic system. The outer stage is a 35 W Stirling cycle cryo-cooler with 2 W of cooling power at 100 K. This is attached to the outermost of three vapor cooled shields which guard the second stage solid-neon cryogen tank. The solid neon system is a 120 liter toroidal tank containing 172 kg of solid neon cooled to below 17 K using liquid helium cooling coils on the ground and space pumping in orbit. This guards the third stage cooling system comprised of 32 l of superfluid helium. The helium tank is suspended on tensioned carbon-fiber straps from a titanium support shell bolted to the solid neon tank. The 17 K guard plus careful control of radiative, conductive, and superfluid film flow heat leaks, keeps the parasitic load on the liquid helium to about 0.8 mW, an astonishing achievement compared to laboratory and earlier space based cryostats. When the additional heat load from operating the ADR is included, the total heat load on the liquid helium is around 1 mW. This gives a projected lifetime of 3.5 yr on orbit for the liquid helium. With the cryo-cooler running at 100% duty



Fig. 14. The XRS instrument during integration and testing prior to mounting on the *Astro-E2* spacecraft. The XRS is an LTD instrument with a four stage cryogenic system composed of a cryo-cooler, solid Ne tank, superfluid helium tank, and a single stage ADR. For scale, the XRS is about 1.2 m tall, and 1.0 m in diameter with a mass of about 400 kg including cryogens. The aperture of the instrument is at the *top of the figure*

cycle, the total cryogen lifetime is around 3 yr, after which the instrument is no longer operational.

The fourth stage of the XRS cryogenic system is a massive single stage ADR using 1000 g of paramagnetic (FAA) salt. The heat leak into the salt pill is dominated by the gas gap heat switch which dumps the cyclic heat of magnetization to the helium bath. The total heat load on the ADR is about $5\mu\text{W}$ giving a 29 h hold time on the ground and about 24 h on orbit when cosmic ray heating of the ADR is included. The 32 pixel silicon microcalorimeter X-ray system only contributes about $0.3\mu\text{W}$ to the total ADR heat load, largely from its separate suspension and wiring layer, the remaining heat load is solely from the accommodation of the refrigerator for spaceflight: its heavy Kevlar suspension, and gas-gap heat switch.

5.2.3 The XRS Detector System

The XRS instrument is based on a silicon microcalorimeter detector that is similar to the detectors used in the XQC but with important distinctions.

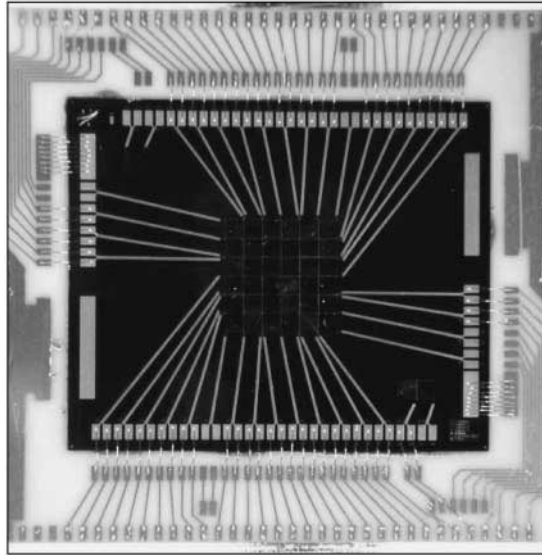


Fig. 15. The XRS microcalorimeter detector array. The array is close-packed in a 6×6 geometry so the pixel suspension system is not visible underneath the HgTe absorbers. The pixels are 0.624 mm square on a 0.640 mm pitch giving a total array field of view of $2.9 \times 2.9 \text{ arcmin}$

The XRS detector array is a two dimensional square array organized in a 6×6 geometry as shown in Fig. 15. There are also two calibration pixels situated in one corner of the detector dice. In the flight system, one of these is wired in place of an edge pixel in the main array. A collimated ^{55}Fe source illuminates the calibration pixel which then provides continuous gain tracking for the detector array. The XRS detector array is a monolithic device, micro-machined out of a silicon-on-insulator (SOI) wafer using a deep reactive ion etching system. The pixels were designed [27] for resonant frequencies above 2 kHz , structural stability against differential contraction, and a thermal conductance of about $4 \times 10^{-11} \text{ W/K}$ at 0.1 K . The resultant pixel design, shown in Fig. 16, was tested as a finite element model, and then modeled and tested in silicon before the array design was finalized.

The XRS thermistors are Mott-hopping conductivity, implanted silicon devices similar to the XQC. The goal is to form a large, uniformly implanted volume, where electrons are thermally assisted from one impurity site to another giving a strong variation in resistance of the device with temperature. In the XQC thermistors, a uniform impurity distribution with depth was attempted using 9 separate implantation doses at varying energies. These were then annealed to form a single uniform implant. Unfortunately, subsequent modeling showed that the implant density varied considerably with depth. This lead to a $1/f$ noise [37] that gave a spectral resolution about 3 times

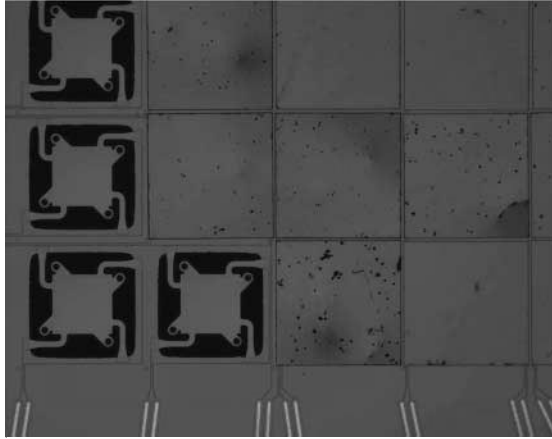


Fig. 16. The partially assembled XRS array. HgTe absorbers have not yet been attached to the pixels on the *lower left*. The pixel structure is micromachined from a single SOI wafer and one can see the pixel suspension structure and the circular mounting posts for the absorber at the edge of each pixel

worse than predicted. To overcome this problem, the XRS devices were made using a new “deep implantation” process where the phosphorus and boron impurities were implanted each with a single dose [27]. The impurities were then diffused throughout the 1.5 μm thick SOI layer to form a uniform, well defined, and thick implanted thermistor. The result is about a factor of two improvement in spectral resolution over the XQC and the original XRS-1 system, both of which were fabricated using the old process.

The bare implanted silicon array is a poor X-ray thermalizer, and thus a separate X-ray absorber is needed [38]. The XRS, like the XQC, uses HgTe, a semi-metal, as an absorber material. An optimal X-ray absorber has a high stopping power (high Z , high density) and a low heat capacity. The high stopping power gives a high quantum efficiency in the smallest possible absorber volume, and the low heat capacity maximizes the spectral resolution. HgTe is a compromise material. While it has a high Z ($Z_{\text{Hg}} = 80$, $Z_{\text{Te}} = 52$) and density ($\sim 8.2 \text{ g/cm}^3$), it has a relatively low Debye temperature ($\sim 140 \text{ K}$) giving a heat capacity of $\sim 0.1 \text{ pJ/K}$ at 70 mK for an XRS absorber. The benefit is that it thermalizes the X-ray interaction energy very efficiently, resulting in minimal, or non-existent, excess line broadening.

The energy resolution of the XRS instrument is about 6 eV at 6 keV and varies only weakly with energy. A spectrum of Mn K_α from the completed flight instrument and Ga K_α from ground calibration of the detector subsystem are shown in Fig. 17, and Fig. 18 respectively.

Equally important to the performance of the instrument is the instrument characterization. This is crucial to extracting the unknown spectrum of a cosmological source from the idiosyncrasies of the observing instrument. The

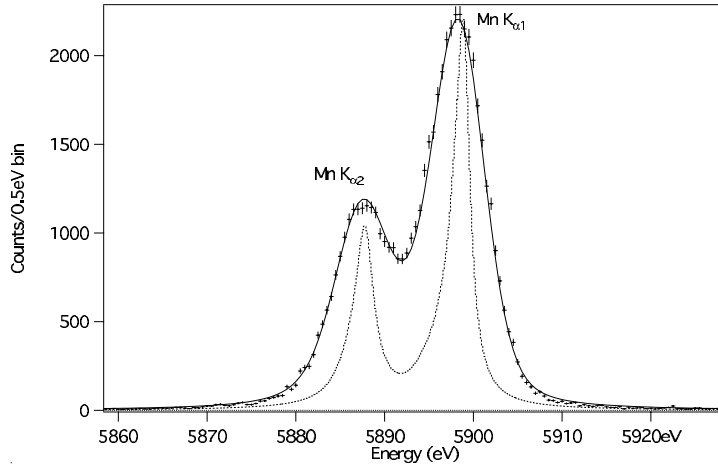


Fig. 17. Mn K_{α} spectrum from an ^{55}Fe internal conversion X-ray source taken with the XRS. The spectrum was taken with the XRS fully assembled and mounted on the XRS spacecraft with the cryo-cooler running at full power. In the spectrum the *dashed line* is the line model from Hölzer [39] and the *solid line* is a fit to the model with an instrumental resolution of 5.7 eV. The data is a summed composite from the XRS array

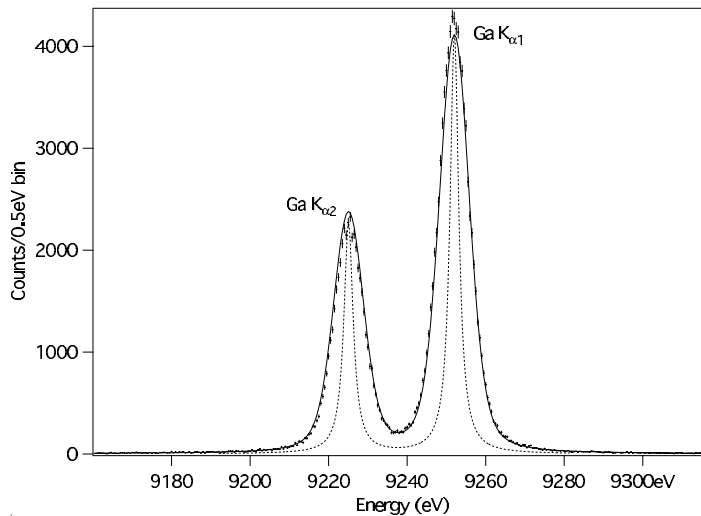


Fig. 18. An XRS spectrum of Ga K_{α} from an X-ray fluoresced GaAs target during ground calibration at NASA/GSFC. The *dashed line* is a two Lorentzian line model and the *solid line* is a fit to the data with an instrumental width of 7 eV FWHM. The data is a summed composite for the XRS array

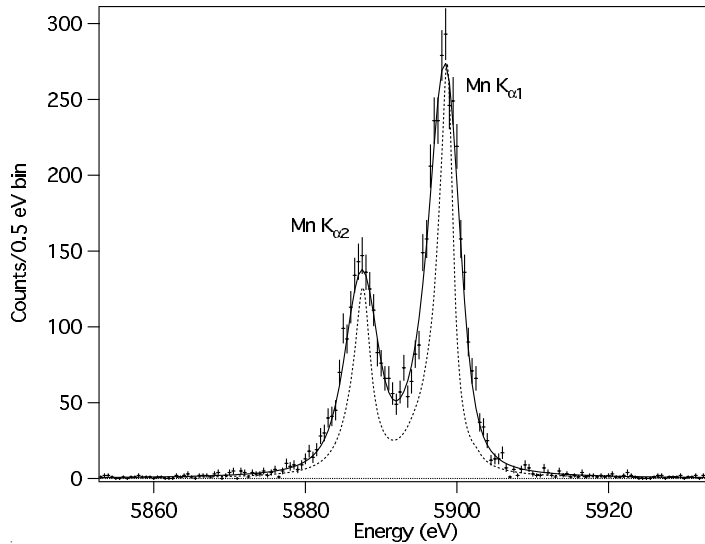


Fig. 19. A spectrum of $\text{Mn K}\alpha$ taken with a laboratory XRS microcalorimeter array with a $0.408 \text{ mm} \times 0.408 \text{ mm}$ absorber. The instrumental width is 3.2 eV FWHM. The base temperature was 40 mK and the detector was biased to about 60 mK

instrument parameters such as quantum efficiency, resolution kernel, spectral redistribution function, gain scale, gain drift recovery, filter transmission, bore-sight alignment, timing accuracy, and imaging half-power diameter, for example, must all be modeled, measured carefully on the ground and in orbit, and then packaged in a manner usable by the observing community. Having a well characterized instrument is at least as important as having a high-performance instrument. The XRS has a detailed calibration program to characterize the instrument both on the ground and in-flight.

It is worth noting that the XRS is only a single example of an implanted silicon microcalorimeter instrument. It is a design constrained by the pixel dimensions, quantum efficiency, speed, and operating temperature of the instrument. The technology, however, is somewhat versatile in trading these parameters for each other. For example, in Fig. 19 we show the results for a similar array to the XRS flight array with smaller $408 \mu\text{m} \times 408 \mu\text{m}$ absorbers operating at a 40 mK heat sink temperature. Here the resolution is improved to 3.2 eV FWHM at 5.9 keV with a 2.9 eV FWHM baseline resolution.

5.3 Future Missions

The XRS and XQC are a first, critical step for LTDs in X-ray astronomy. They are, however, merely a first step. The next set of observatories that will succeed *Chandra*, *XMM-Newton*, and *Astro-E2* will necessarily be more complex and put great demands on the cryogenic detector community if the

technology is to find a place on these observatories. Currently there are three major observatories that are in the planning stages and have a cryogenic X-ray instrument as part of the focal plane. These observatories must be significantly more powerful than the current observatories to be compelling investments for the scientific community and the government organizations that fund them.

Currently on the drawing board, roughly in order of launch schedule are the Japanese (ISAS/JAXA) *NeXT* mission, NASA's *Constellation-X*, and the European Space Agency's *XEUS*. National boundaries are routinely crossed in the construction of large observatories so that each of these missions will probably be constructed by large international consortiums. In addition, large observatories tend to change considerably from their early planning stages to their final launch configuration, sometimes merging, and sometimes separating into smaller payloads. Thus our discussion of these missions, should serve to illustrate the direction and challenges for the LTD community and not as a prediction of the final form any of these missions will take.

Table 1. Comparison of future large X-ray observatories showing some of the parameters important for low temperature detectors. The requirements shown are approximate, and for illustrative purposes only

	NeXT [‡]	Constellation-X [‡]	XEUS [‡]
Effective area (1 keV)	1000 cm ²	15 000 cm ²	60 000 cm ²
Focal length	9 m	10 m	50 m
Half power dia.	30''	15''	5''
Spectral resolution	5 eV at 6 keV	2 eV at 1 keV 4 eV at 6 keV	2 eV at 1 keV 5 eV at 8 keV
Pixel size	0.5 mm	0.25 mm	1 mm
Operating temp.	< 100 mK	< 100 mK	< 100 mK
Array size	30 × 30	30 × 30	30 × 30
Field of view	5'	2.5'	1'
Cooler	cryogen-free	cryogen-free	cryogen-free

[‡]www.astro.isas.jaxa.jp/future/NeXT

[‡]constellation-x.gsfc.nasa.gov

[‡]www.rssd.esa.int/XEUS

A summary of some of the characteristics of the three planned observatories are shown in Table 1. The general emphasis is on spectroscopy and very large collecting areas using very large X-ray optics. The *Constellation-X* mission, for example, will have almost 100 times more collecting area than the XRS. Similar expansions in capability are expected from the LTD community for these missions. The requirements in Table 1 include significant improvements in the detector design over the XRS in every respect: 30 times the pixel count, smaller pixel size, three times the spectral resolving power,

and a significantly higher throughput. This must all be accomplished in a smaller package and with a long lifetime, fully cryogen-free system.

The development work for these instruments drives nearly all progress in X-ray LTDs. There is little synergy with commercial applications so the entire development burden must be borne by future X-ray missions. Nearly all types of LTDs are still under consideration for the focal planes of these instruments including semiconductor, TES, and magnetic microcalorimeters, superconducting tunnel junctions, and kinetic inductor detectors. It is not clear which of these systems will actually make it into the final instruments, but what is clear is that this will not be a simple extension of the technology used in the XRS instrument. There must be a fundamental shift in development and assembly of cryogenic X-ray detectors. While the XQC and XRS are hand-assembled, and hand wired systems, this is not possible with 1000+ pixels and readout channels. Monolithic assembly techniques will be required. In addition, the cryogenic staging and complex wiring layers for 1000 discrete amplifier channels is probably not tractable in a compact instrument. A pixel multiplexing scheme is probably required. Several schemes are currently under consideration, including a time division multiplexed system [40] and a frequency division system [41]. In a time division multiplexer each channel in a column is sampled periodically in a round-robin fashion. In a frequency division multiplexed scheme each channel occupies its own part of the overall amplifier bandwidth.

Finally, future missions will require a low temperature refrigerator to cool the detectors to below 0.1 K. This must also interface with the base temperature and cooling power of the mechanical cryo-cooler. If the base temperature is more than a few degrees Kelvin, this will require a complex multi-stage ADR, using multiple refrigerants, magnets, and heat switches. In planning future LTD instruments it is important to remember that the “off” conductance of the heat switch sets the scale for the entire ADR as it sets the minimum cooling power that must be achieved by the ADR’s refrigerant. This in turn dictates the cycle time, the size of the magnet, and for magnetically sensitive detectors, the mass of the magnetic shielding. The XRS represents one point in this multi-dimensionally phase space, using the largest ADR refrigerant ever built to account for the high off-conductance of the gas gap heat switch. Future, compact instruments, including the next generation observatories discussed here, will need to find other designs that use much smaller refrigerants with smaller heat switches that have lower parasitic heat loads.

6 Laboratory Astrophysics and LTDs

The benefits provided to the astrophysics community by LTDs are not limited to sounding rocket experiments or X-ray observatories, but extend to ground-based measurements of astrophysically relevant X-ray spectra. For

these studies, engineering models and flight spare equipment are being retrofitted to operate in the laboratory. LTDs have become the highest resolution non-dispersive spectrometer available for laboratory studies of astrophysically relevant X-ray emission. Thus, the development of high resolution LTDs is multi-faceted, providing both the means for measuring spectra from extra-solar objects, and also the means for their reliable interpretation. Here we describe the use of LTDs for X-ray laboratory astrophysics.

6.1 Instruments for Laboratory Astrophysics: LTDs and Electron Beam Ion Traps

X-ray spectroscopy, as discussed in Sect. 2, provides the means for understanding the nature of non-terrestrial sources through a range of spectral diagnostics. The utility of these diagnostics requires knowledge of large sets of atomic data that describe the physics of the X-ray emission. Minimizing the uncertainty and establishing reliable error estimates associated with these data are paramount to their reliability and utility. Historically, testing of atomic data has been accomplished through a symbiotic relationship between theory and experiment: theoretical calculations produced large data sets, while experiments provided benchmarks to test and guide the theory. Because experiments often only covered a small portion of parameter space, testing entire atomic data bases was impossible. Over the past decade, however, more advanced experimental facilities have come online that are able to measure complete sets of atomic parameters in finite amounts of time. These facilities have the capacity to address specific problems facing the interpretation of astrophysical spectra. Experiments conducted specifically to address astrophysical problems are generally referred to as “laboratory astrophysics”. Laboratory astrophysics encompasses many different fields including the study of dust particles, optical spectra, UV spectra, and X-ray spectra [42]. In support of X-ray missions, laboratory X-ray astrophysics experiments are being conducted at several advanced facilities world-wide including, electron beam ion traps, heavy-ion storage rings, electron-cyclotron resonance facilities, and tokamaks. For a review of laboratory X-ray astrophysics see [43].

Low temperature detectors have been instrumental in laboratory astrophysics studies. Although LTDs have been tested earlier at LLNL [44] and some measurements at other facilities have been conducted [45, 46], it was not until the XRS/EBIT microcalorimeter spectrometer was installed on the LLNL EBIT-II in 2000 that LTDs have been routinely used as part of a laboratory astrophysics program [47, 48]. Here we give a brief description of the LLNL EBITs, the XRS/EBIT microcalorimeter spectrometer used at LLNL, and some examples of laboratory astrophysics measurements where the XRS/EBIT is used.

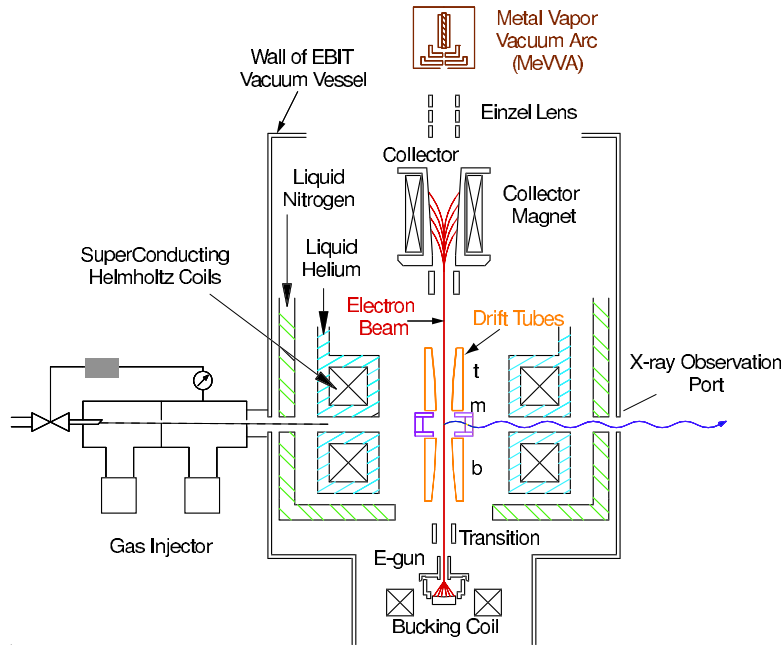


Fig. 20. Sketch of the layout of the Lawrence Livermore National Laboratory electron beam ion trap. Courtesy of Klaus Widmann

6.1.1 The Electron Beam Ion Trap

An electron beam ion trap (EBIT) is a device used to study the atomic physics governing the emission of radiation from highly-charged ions [49, 50, 51]. An EBIT consists of three major parts: a mono-energetic electron beam, an electrostatic trap, and a collector. The electron beam is used to create, excite, and trap ions in the radial direction. The electron beam travels from the electron gun, located near the bottom of EBIT, through the trap region and then terminates on the collector. The trap consists of three drift tubes that confine the ions electrostatically along a 2 cm portion of the electron beam. In the trap, the electron beam is compressed to a diameter of $\sim 60 \mu\text{m}$ by the magnetic field created by a pair of superconducting Helmholtz coils. Figure 20 shows a sketch of all the major components of the EBIT.

Ions are injected into the trap using either a metal vapor vacuum arc (MeVVA), or a ballistic gas injector. The MeVVA uses an arc discharge to ablate low-charge-state ions from the cathode material. The ions are subsequently transferred electrostatically to the trap region. The ballistic gas injector uses differential pumping to inject a collimated stream of neutral material into the trap. Once the stream intersects the electron beam the neutral atoms and molecules are ionized and trapped. To avoid the accumulation

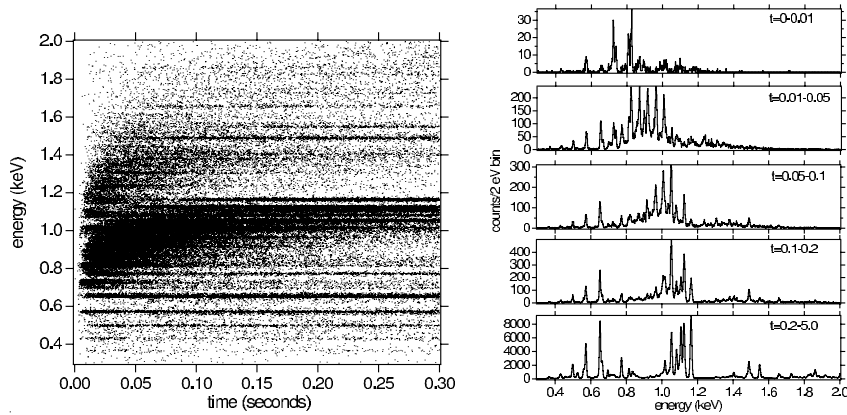


Fig. 21. Time resolved iron spectra emitted from the LLNL EBIT-II. The electron beam energy was 4.5 keV. The figure on the *left* shows the first 300 ms of a 5 s timing cycle. Equilibrium is achieved at ~ 200 ms. The time selected spectra on the *right* demonstrate the evolving charge balance as a function of time

of background ions, the trap is emptied and replenished on a periodic timing cycle. A single cycle typically lasts a few seconds.

Once trapped, ions are ionized to the desired charge state by the mono-energetic electron beam. The time required for the trapped ions to reach equilibrium depends on the desired charge state and the conditions of the trap. Using time-resolved spectroscopy, it is possible to study the ionizing portion or the equilibrium portion independently. Without time resolution, measured spectra contain blends of ionization stages that can lead to confusing results. Figure 21 shows a time resolved spectrum of 10 000 phase-folded EBIT injection cycles with accompanying time-selected spectra. This figure shows the significant difference in ionization balance as a function of cycle time.

Access to the trap is granted through six axial ports directed towards the trap region. Five of these are used for spectroscopy, and the sixth is used for the gas injector. A seventh port looking down into the trap region houses the MeVVA. The electron beam enters through a port on the bottom. To reduce systematic errors and to provide high-resolution spectra over specific bandwidths, more than one spectrometer is used for each measurement. A typical arrangement of spectrometers attached to the LLNL EBIT is given in Fig. 22.

EBITs have operational parameters making them well suited for laboratory astrophysics. Because the electron beam is nearly mono-energetic with an energy spread of only 20–50 eV, it is possible to measure X-ray emission from nearly pure ion states, making it easy to identify lines from a specific charge state and to probe specific atomic processes. Typical electron densities in the trap are $10^{10} \leq n_e \leq 10^{13} \text{ cm}^{-3}$ similar to those found in many astrophysical plasmas. The two EBITs, EBIT-I and Super-EBIT, currently

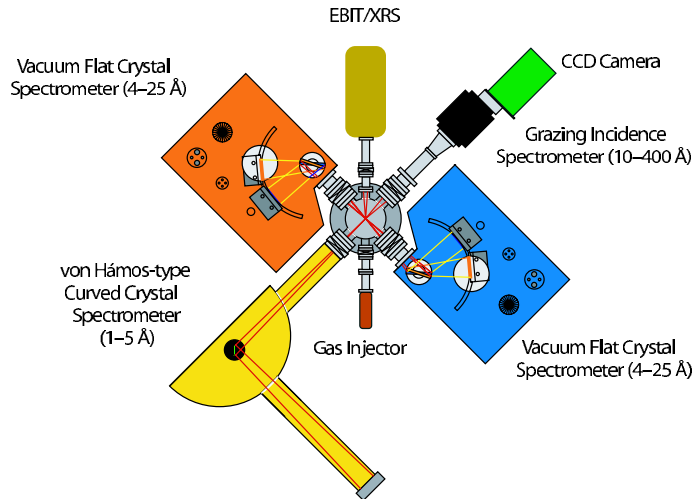


Fig. 22. Top down view of a typical spectrometer arrangement on the LLNL EBIT-I. In addition to the XRS/EBIT, are two flat crystal spectrometers, a curved crystal spectrometer, and a grazing-incidence spectrometer

operating at LLNL, have a combined operational electron beam energy range from below 100 eV to above 200 keV, making it possible to study all astrophysically relevant ions as well as truly high- Z , highly-charged ions up to bare uranium, U^{92+} . The LLNL EBITs have also been used to produce spectra from Maxwellian plasmas [52] so that thermal plasmas in coronal equilibrium can be studied. In addition, by rapid switching of the electron beam energy, X-ray spectral signatures from photoionized plasmas can be produced [53].

6.1.2 The GSFC Microcalorimeter Detector For Laboratory Astrophysics

Two different NASA/GSFC microcalorimeter arrays have operated at the LLNL EBIT facility. The first was based on the *Astro-E1* design. The second array was assembled in the same fabrication run as the *Astro-E2* flight instrument. The *Astro-E1* array had a resolution of ~ 8 eV below 1 keV and ~ 11.5 eV at 6.7 keV. As stated in Sect. 5, the *Astro-E2* array has a resolution of 6 eV at 5.9 keV.

Both arrays utilize the same detector support system used in the *Astro-E2* flight instrument. The system has readout electronics for 32 channels, including pulse height and pulse shape analysis, pile-up detection, and noise analysis. The detector system time tags X-ray events to 10 μs precision using a GPS timing system to correlate the X-ray event times with the EBIT timing cycle. This makes it possible to perform detailed studies of both equilibrium and non-equilibrium plasmas.

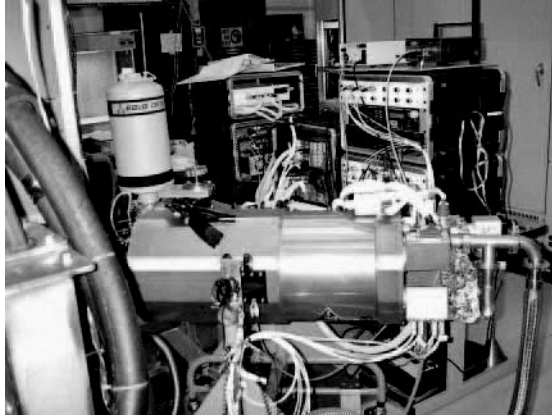


Fig. 23. Photograph of the XRS/EBIT on LLNL's EBIT-I. Notice the pumping line on the back (*right side*) of the photograph. Read out electronics and thermometry can be seen in the background

The dewar system is a standard laboratory liquid helium cryostat adapted to accept a small ADR developed for the XQC described in Sect. 5. The typical hold time of the ADR is between 12 and 14 h at a control temperature of 60 mK. Temperature control of the detector assembly is achieved using commercial doped germanium thermometers read out by a high performance resistance bridge and a software PID controller. The PID controller provides live feedback to the superconducting magnet that controls the temperature of the ADR. At 60 mK, temperature control of $\leq 1 \mu\text{K}$ RMS is consistently achieved. This cryostat accepts the *Astro-E2* engineering model detector assembly which is axially aligned with the X-ray port on the bottom of the cryostat, hence, the dewar is rotated horizontal when it is connected to one of the six axial X-ray ports on EBIT. The cryogen ports are offset so that the cryogenes can be filled and the ADR can be operated while the dewar is horizontal. In this configuration the liquid helium bath is pumped to 1.5 K. Six liters of helium lasts 36–48 h. A photograph of the XRS/EBIT attached to EBIT-I is given in Fig. 23.

As in any low temperature detector, the array must be shielded from UV and thermal radiation, and photon-induced shot noise created by optical radiation. This is accomplished with four blocking filters, each made of $\sim 1000 \text{ \AA}$ of polyimide coated with $\sim 1000 \text{ \AA}$ of aluminum, each located at a different thermal interface. A fifth filter is used to separate the vacuum of the XRS/EBIT ($\sim 10^{-8}$ Torr) from that of EBIT ($\leq 10^{-11}$ Torr). This filter is mounted on a manual gate valve and is easily interchangeable. Typical materials for the vacuum isolation filter are parylene, beryllium, and polyimide. To ensure the integrity of the blocking filters and to account for any oxidation that may occur on the aluminum surfaces, the transmittance of

the blocking filters was measured as part of the *Astro-E2* filter calibration program [54, 55]. Once the XRS/EBIT is attached to EBIT and at its operating temperature, the condition of the filters is verified by illuminating the XRS/EBIT with a continuum of X-rays produced by an X-ray tube attached to the opposite viewport. Significant changes in absorption edge strengths, such as the oxygen edge or the aluminum edge, are indicative of a change in filter response.

6.2 Measurements Using the XRS/EBIT at the LLNL EBIT Facility

The XRS/EBIT has become a standard instrument used for a variety of experimental studies. For example, with the Maxwellian simulator mode [56], the XRS/EBIT has been used to measure spectral signatures of Maxwellian thermal plasmas. It has been used for transition rate measurements [57], and to measure X-ray emission from non-equilibrium ionizing plasmas. Described below are two examples of where the XRS/EBIT spectrometer provided new measurement capabilities: measuring absolute cross sections of Fe L-shell X-ray transition, and measuring X-ray emission from charge exchange in the study of cometary atmospheres.

6.2.1 Measuring Electron Impact Excitation Cross Sections of X-ray Transitions

As mentioned in Sect. 2, the line strengths of radiative transitions depend on several different atomic parameters and plasma conditions. One atomic parameter fundamental to the diagnostics of coronal plasmas is the radiative electron-impact excitation (EIE) cross section. EIE cross sections determine the strength of X-ray lines in collisional equilibrium. A multitude of calculated EIE cross sections are available, but because experimental data is sparse, many of the calculations remain unchecked. Measurements of the total excitation cross sections including non-radiative contributions, and low energy indirect excitation processes are measured using merged beam techniques [58, 59]. Also, cross sections of low charge states have been measured using crossed beams [60]. However, measurements at the LLNL EBIT are the only ones that provide EIE cross sections for radiative transitions in highly-charged ions for the direct interpretation of astrophysical spectra.

Using the LLNL EBITs, absolute EIE cross sections are measured by recording the X-ray emission from EIE and radiative recombination (RR) simultaneously. Then, by normalizing the emission from EIE to the well-known cross sections for RR, the EIE absolute cross section can be determined. For this technique to be successful, the RR and EIE spectral features corresponding to the same ion must be resolved. Otherwise, it is not possible to eliminate the electron beam-ion overlap integral that defines the emitting volume. For

astrophysically relevant X-ray emission, this is achieved by taking advantage of EBIT's narrow electron beam and the properties of the XRS/EBIT as described below.

Radiative recombination is the inverse process of photoionization and occurs when a free electron is captured by an ion into a bound state. In contrast to the RRC emitted from photoionized plasmas, RR radiation emitted from EBIT creates discrete spectral features whose energy is equal to the sum of the electron beam energy and the binding energy of the recombined state. The width of the RR feature emitted from EBIT is, therefore, equal to the beam width. The RR spectral features are very weak compared to direct excitation features because the cross sections for RR are ~ 1000 times smaller.

The properties of radiative recombination create several requirements that must be met to measure the emission from RR and EIE simultaneously. First, the RR emission must be resolved. This can be problematic for several reasons. The finite Gaussian energy profile of the electron beam combined with the proximity of the ionization potentials of different ionic species makes it possible for neighboring ionization species to be present. Also present are ions of indigenous background gases. Thus, depending on the convolved width of the instrumental profile and the beam profile, blending of RR features from different ions may occur. Low resolution instruments that significantly broaden the RR features limit measurements to higher- Z ions where differences in binding energies between the ions are larger. This requirement also means the spectrometer must have adequate time resolution to prevent the non-equilibrium portion of the timing cycle from contaminating the measurement.

The second and third major requirements are large bandwidth and large collection area. A large bandwidth is necessary because the accuracy of RR cross sections is better at high electron energies, and at these energies RR spectral features may appear at energies several keV above direct excitation features. A large collecting area is necessary in order to allow the detection of the weak RR features. This precludes the use of dispersive spectrometers because the reflection efficiencies of crystals and gratings are too small.

The first measurements of EIE cross sections at the LLNL EBIT facility used solid state detectors [62, 63, 64]. However, because of the low energy resolution of the detectors only the cross sections of K-shell transitions or high- Z ions were measured. This problem is solved with the XRS/EBIT. The wide bandwidth, large collecting area, excellent time resolution, and ~ 10 eV energy resolution made the measurement of absolute cross sections of Fe L-shell X-ray transitions possible for the first time.

Absolute cross sections of several Fe L-shell X-ray lines from Fe XVII–XXIV have been measured using the XRS/EBIT [61, 65, 66] including X-ray transitions in Fe XVII–XXIV. As an example, Fig. 24 shows the X-ray emission from Fe XVII measured by the XRS/EBIT at EBIT-I [61]. Notice the strong direct excitation line emission along with the relatively weak emis-

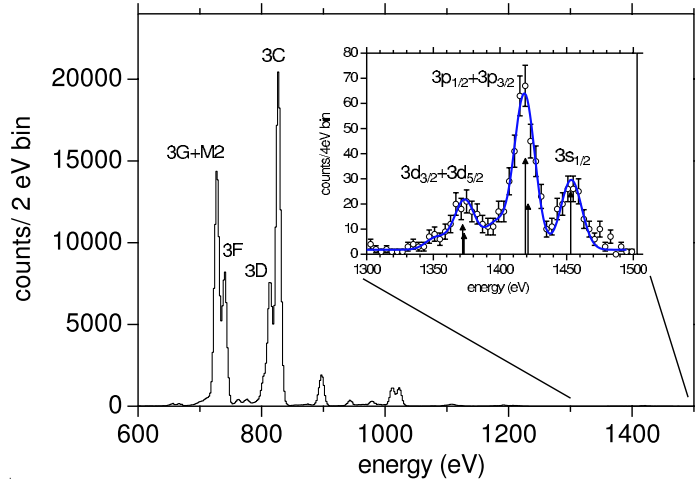


Fig. 24. Spectrum of Fe XVII measured by the XRS/EBIT microcalorimeter spectrometer. The *inset* shows the energy range containing the photons from radiative recombination. They represent the recombination into different fine structure components of Fe XVII. From the RR features, the electron beam energy is determined to be 964 eV with a FWHM of ~ 20 eV. This figure is from *Brown et al.* [61]

sion from RR shown in the inset. The width of the electron beam for this measurements was ~ 20 eV.

6.2.2 The Study of X-ray Emission Following Charge Exchange Recombination for Diagnosing Cometary Plasmas

In 1996 X-ray emission from comet Hyakutake was discovered in observations by *ROSAT*. Subsequently, X-ray emission from other Comets has been observed such as Linear C/1999 S4 and McNaught-Hartley [67]. The accepted mechanism for the X-ray radiation is charge exchange recombination (CEX). Charge exchange, in this case, is the radiationless transfer of a bound electron from a neutral atom in the comet to an upper level in an ion from the solar wind. The ion stabilizes radiatively by emitting an X-ray.

Just as in other realms of X-ray spectroscopy, the diagnostic utility of CEX X-ray emission relies on the accuracy of the atomic data used to interpret the spectra. Although studies of charge exchange have taken place for decades [68], most have focused on ion-neutral collisions with energies greater than 50 keV/amu. In contrast, the predicted interaction energy between cometary neutrals and solar wind ions is less than 3 keV/amu (~ 800 km/s) [69]. Theoretical models of charge exchange emission have made significant progress, especially since the discovery of cometary X-ray emission [70, 71], but they remain largely untested and incomplete.

Charge exchange following low-energy ion-neutral collisions for diagnosing solar wind-comet interactions is currently being studied at the electron cyclotron resonance (ECR) facility at NASA's Jet Propulsion Laboratory and at the EBIT facility at LLNL. At the ECR, ion-neutral collisions with interaction velocities of ~ 800 km/s are being studied [72, 73], corresponding to the high-velocity solar-wind ions. The LLNL EBIT experiments are complementary, covering the low velocity range below 100 km/s corresponding to the velocities of solar wind ions in the inner region of a comet [74]. LTDs have played a significant role in the study of charge exchange emission at the LLNL EBIT.

X-ray emission following charge exchange recombination is studied at the LLNL EBIT facility using the magnetic trapping mode [75]. In this mode, instead of being trapped radially by the potential of the electron beam, the ions are trapped by the 3 T magnetic field produced by superconducting Helmholtz coils in the EBIT. Together with the electrostatic trapping by the drift tubes, this system acts like a Penning trap. Neutrals are either pulsed or continuously injected into the trap using the gas injector. When the electron beam is off, the ion cloud expands and it no longer acts as a slit for dispersive grating and crystal spectrometers. A non-dispersive spectrometer is therefore required.

High-purity germanium detectors with resolutions between 120 and 180 eV were used in the first charge exchange measurements at the LLNL EBIT [76, 77]. For these experiments, X-ray emission following charge exchange reactions between hydrogenic Ne, Ar, Kr, Xe, Au, U and neutral Ar, CO₂, Ne, are measured. The results of these measurements demonstrated that for low energy collisions, X-ray emission from high- n Rydberg states is unusually strong compared to those occurring after high-energy collisions. The figure of merit to determine the interaction energy is the ratio of the $n \geq 3 \rightarrow 1$ transitions relative to the $2 \rightarrow 1$ transitions, known as the hardness ratio. For low energy transitions the hardness ratio is high, and for high energy interactions the hardness ratio is low.

Using the XRS/EBIT at LLNL, X-ray emission from charge exchange between C⁵⁺, C⁶⁺, Ne⁸⁺, Ne⁹⁺, Ne¹⁰⁺, O⁷⁺, O⁸⁺, with neutral Ne, CO₂, CH₄, and alcohol, were all measured. Figure 25 shows the spectra measured after charge exchange occurs between O⁸⁺ and either ethyl alcohol, methane, or carbon dioxide. The order of magnitude improvement in resolution compared to the germanium detector provides many new results. For example, strong line emission from the high- n Rydberg transitions, and the spectral dependence on the neutral gas and different ion species is readily apparent. In addition, the significant contribution from double capture was discovered in these experiments [78]. Just as the name suggests, double capture occurs when two electrons are transferred to the ion as opposed to one. In Fig. 25, the signature of double capture is most apparent in the the spectrum of O⁸⁺ interacting with alcohol. This results in strong emission from $n = 3 \rightarrow 1$ and

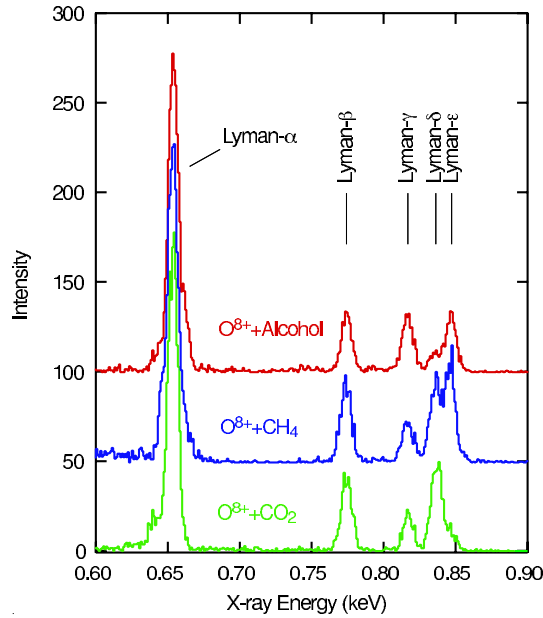


Fig. 25. Spectrum of X-ray emission produced after charge exchange between bare O^{8+} and different neutral gases using the XRS/EBIT. This demonstrates that it is possible to detect different gas constituents from a CEX spectrum and that contributions from double electron capture must be taken into account when modeling X-ray emission from charge exchange. This figure is reproduced from *Beiersdorfer et al.* [78]

$n = 4 \rightarrow 1$ transitions. This signature is unobservable at the resolution of a typical solid state detector.

Figure 26 shows the spectrum from the comet C/Linear 1999 S4 [79] observed with the *Chandra* ACIS CCDs. The lower panel shows the superposition of the spectra measured by the XRS/EBIT of helium-like and hydrogenic C, N, and O after charge exchange with CO_2 . This comparison clearly shows the stark improvement in the spectral information provided by LTDs compared to solid state detectors. In addition, the laboratory data shown here were used to successfully fit the *Chandra* data demonstrating that charge exchange alone can account for all the X-ray flux emitted from a comet. Importantly, the laboratory data can be used to fit astrophysical spectra directly, with no reliance on theoretical databases [78].

The launch of *Astro-E2* in early 2005 will make possible the first high-resolution measurement of the cometary X-ray emission. Two observations are scheduled: the comet 9P/Tempel on July 4, 2005, and comet 73P/Schwassmann–Wachmann 3 in 2006. The factor of nearly 20 improvement in spectral resolution compared to *Chandra* will surely present new insight in to the physical processes taking place in the atmospheres of comets.

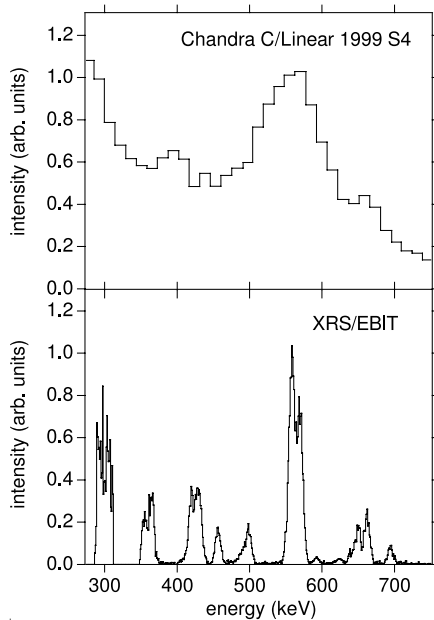


Fig. 26. X-ray emission spectrum measured from the comet C/Linear 1999 S4 using the *Chandra* ACIS-S and the charge exchange induced spectrum measured at LLNL EBIT-I using the XRS/EBIT. The XRS/EBIT spectrum is the superposition of six separate spectra of charge exchange induced emission from hydrogenic and helium-like C, N, and O. For a complete explanation of these data see *Beiersdorfer et al.* [78]

More importantly, because this emission is a diagnostic of the ionization balance, composition, and velocity of the solar wind ions, it can be used to remotely observe the properties of the solar wind throughout the solar system. *Astro-E2* will also observe other objects that show evidence for CEX emission, such as stellar winds, the galactic center, the galactic ridge, the cosmic X-ray background, and supernova remnants to name a few. The continued CEX studies in the laboratory will provide a significant contribution to the interpretation of these data.

7 Future Challenges

What astrophysicists want is an observatory with a large field of view, very fine spatial and spectral resolution, a very large effective area, and the ability to handle bright sources with precision timing. Future CCD instruments can and will provide the large field of view and fine spatial sampling in a single instrument, and future X-ray telescopes will provide the large collecting area. What is missing is the high spectral resolution and the ability to handle high

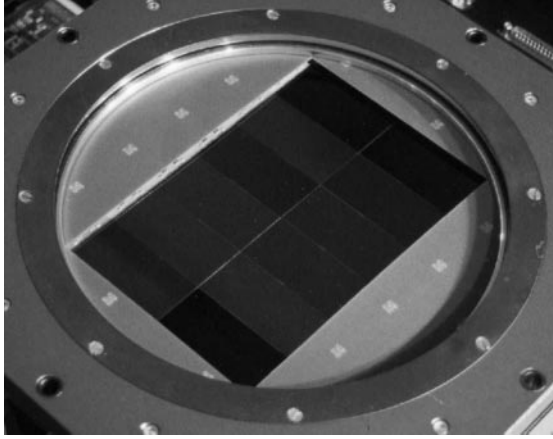


Fig. 27. An example of a large-scale CCD camera is the CFH12K CCD camera used at the focal plane of the Canada-France-Hawaii telescope on Mauna Kea in Hawaii. The CCD camera is $12\,288 \times 8192$ pixels or over 100 megapixels. Reprinted from *Cuillandre et al.* [80]

count rates with precision timing. This is what the astrophysics community expects from low temperature detectors. The difficulty is that low temperature detectors are not CCDs. They don't scale the same way and present profoundly different challenges and problems in implementation.

The instrument scientist must face the very real problems of scaling today's ~ 30 pixel arrays to the megapixel arrays needed for future instruments. This is a non-trivial task, and each order of magnitude expansion in the number of pixels brings daunting challenges to the detector design and instrument implementation.

7.1 Scaling Limits in Current LTD Technologies

Scaling today's small arrays of X-ray LTDs to large arrays that cover square centimeters or more of focal plane area present very real problems in detector and readout design. CCDs scale well because the packet of charge induced by an X-ray can be serially clocked out from the center of a large detector. Scaling CCDs to large area depends on developing high fabrication yields, producing 3 and 4 side abut-able sub arrays, and increasing the speed at which the induced charge can be clocked out of the array without loss. As an example, Fig. 27 shows the huge 100 megapixel CFH12K optical CCD camera operating on the Canada-France-Hawaii Telescope on Mauna Kea. LTDs do not scale this way. There is no equivalent to the CCD charge transfer mechanism for LTDs where most devices operate calorimetrically. The heat induced by an X-ray interacting with an LTD cannot be "clocked out" of the LTD array.

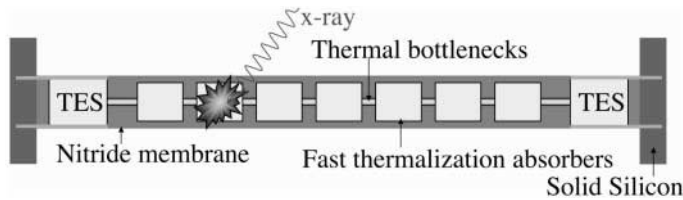


Fig. 28. A recent imaging microcalorimeter detector developed at NASA/GSFC [83]. The Position Sensitive TES (PoST) detector uses two TES thermometers to read out a linear array of pixelated absorbers. This allows a number of “effective pixels” to be read out using only two readout nodes

So how does one scale LTDs from the 32 pixel XRS to substantially more channels? One solution is to simply increase the number of readout channels. However, as in XRS, each readout node implies a low temperature amplifier (FET or SQUID) and a wiring layer that extends from the pixel to the low temperature amplifier and then to room temperature. People have envisioned, although not attempted, systems with up to 1000 discrete readout channels. The HAWC infrared instrument on the SOFIA airborne observatory uses 384 FET channels to read out an infrared bolometer array at 0.2 K [81]. However, using such a brute force system for a large array of X-ray detectors with a base temperature of 0.05 K and in a space environment would present serious difficulties including the thermal staging of the FETs, the extremely complex wiring layer, and the very large number of discrete room temperature amplifiers.

To scale to very large arrays it is necessary to break the one-to-one correspondence between readout nodes and imaging elements on the detector array. One method, as we have discussed, involves a multiplexed row-column readout. This allows all the channels of one column of devices to be combined into one readout node. The number of readout nodes then only scales as the number of columns N in an $N \times N$ array. The number of elements per column, however, is limited. The time and frequency division multiplexing schemes envisioned for *Constellation-X* and *XEUS* are limited by, among other things, the bandwidth of the low-temperature SQUID amplifier. In addition, the number of readout nodes is also limited by the power consumption at low temperatures, and the complexity of the wiring layer. A reasonable limit for scaling on these two axes would be of order 100 channels per readout node and of order 100 readout nodes per instrument. This is possible *in principle*, probably with some compromises in the detector speed, and gives a reasonable scaling limit for these two axes for the foreseeable future. However, the current requirements for *Constellation-X* and *XEUS* are an order of magnitude less with 32 columns and 32 readout nodes, and even this has not yet been demonstrated.

To reach megapixel scales, the number of channels must be increased using a fundamentally different approach. One method originally pioneered by

Krause in superconducting tunnel junctions [82] and recently demonstrated for TES based microcalorimeters [83] is to create LTDs with intrinsic spatial information. This allows one to divide up a discrete “pixel” into a larger number of “effective pixels” with some discriminating parameter to convey the location of the X-ray event within the “pixel”. An example of a position sensitive TES (PoST) microcalorimeter is shown in Fig. 28. In this configuration two readout nodes are used to locate the X-ray event in a linear array of segmented absorbers. The relationship between the event on the two readout nodes (relative timing, relative pulse shape, etc...) gives the position, and the sum the energy of the event. One could also envision this same type of scheme in two dimensions with four readout nodes locating the X-ray event in a plane of X-ray absorber(s). There are limitations to this scheme, however. In most cases the energy resolution degrades with the number of “effective pixels”. In addition, the pile up limits for each pixel do not increase as the pixel is subdivided into imaging elements. Thus the X-ray throughput per imaging element decreases as the number of imaging elements per “pixel” is increased. The benefit is, of course, another effective axis for increasing the pixel count. Figure 29 shows the increase in field of view of a *Constellation-X* instrument with the same number of multiplexed rows and columns (32 by 32) but with 10 imaging elements per node, giving 10^4 total imaging elements. The increased field of view drastically increases the observing efficiency of the observatory for extended objects and allows for the discovery of serendipitous sources within the larger observed field.

To continue with our scaling limits, we now have three axes: the number of readout nodes, the number of pixels per readout node, and the number of imaging elements per pixel. Again, reasonable limits for each axis are of order 100 giving an effective 1 megapixel imaging detector system, at least in theory, and with some compromises in spectral resolution and throughput. There are, however, immense implementation problems that we have not addressed including managing the heat produced in a close-packed array, developing the on-chip wiring layer, and producing high-yield, uniform device arrays. It will be interesting to see if this approach alone can yield a megapixel sized flight-qualified array with reasonable parameters.

To scale still further either requires additional compromises or a fundamental shift in how the device readout is accomplished. One possibility is to reduce the requirements on spectral resolution and combine pixels electrically in a row-column readout. Since the noise of the detectors is uncorrelated, the energy resolution will scale as the square root of the number of pixels combined per readout node. Thus one could increase the pixel count by an order of magnitude simply by combining channels, although with a factor of three lower spectral resolution.

The future for truly large scale LTDs probably lies in substantially increasing the number of multiplexed channels by significantly increasing the bandwidth of the connection between the low temperature amplifiers and the

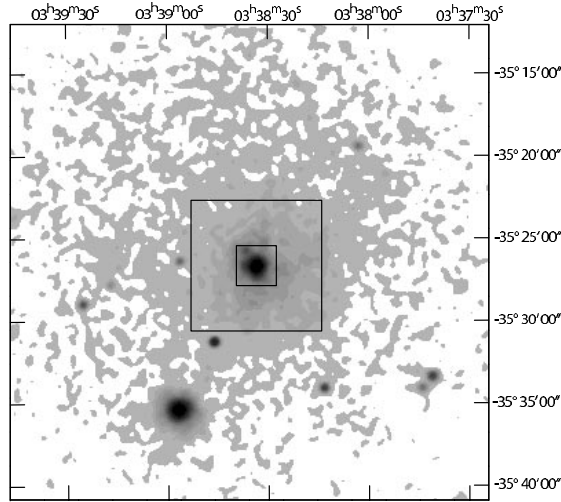


Fig. 29. A *ROSAT* image of NGC1399 a galaxy in the center of the Fornax cluster of galaxies. The *central square* denotes the standard *Constellation-X* field of view for a 32×32 pixel detector array. The *outer square* shows the field of view using the same number of readout channels but using a position-sensitive detector array with 10 “effective pixels” per read-out node

room temperature electronics. Recently NIST-Boulder, has demonstrated a microwave SQUID frequency division multiplexing scheme [84] that could dramatically increase the number of multiplexed nodes per readout channel. Another important recent advance is the development of the microwave kinetic inductor detector [85]. The microwave kinetic inductor X-ray detector forms each detector into a microwave resonant circuit with very high Q . In principle, a very large number of channels with different resonant frequencies can then be combined on a single high bandwidth cable out of the cryostat. These or similar future developments are needed if we are to break out of the complex, and extremely limiting scaling rules for low temperature detectors.

7.2 Where Do We Go From Here? Future Missions, Dreams, and Challenges

The future of LTDs for X-ray astronomy is both exciting and daunting. The success of the XQC instrument and the imminent launch of the XRS are truly seminal moments for LTDs and for X-ray astronomy. This is the beginning of high-resolution spectroscopy with true spatial-spectral imaging. The next step, however, is truly daunting. There are huge technical challenges in developing the 1000+ pixel, high-resolution, high-throughput focal plane instruments for *NeXT*, *Constellation-X* and *XEUS*. These instruments, however, represent only the short-term challenges. To quote from the 2003

NASA/SEU (Structure and Evolution of the Universe) Road-map: “Thirty by thirty arrays of microcalorimeters are envisioned for *Constellation-X*, but such small array have very limited fields of view. Future missions will need much larger arrays” [86].

Future “vision” missions in NASA’s *Beyond Einstein* program include *MAXIM*, a microarcsecond X-ray interferometer, and *Generation-X*, a very large collecting area, 0.1 arcs X-ray observatory. Both of these missions will require very large format arrays of small 20 μm pixels. We as instrument scientists must look beyond our current challenges to come up with new ideas for large arrays. We as astrophysicists, however, must be mindful of the problems, challenges, and resources this development requires.

The ability of LTDs to gain and maintain a place on future missions will depend on our ability to innovate and keep pace with the requirements of ever more powerful X-ray observatories.

References

- [1] R. Giacconi, H. Gursky, F. R. Paolini, B. B. Rossi: Phys. Rev. Lett. **9**, 439 (1962). 359, 369
- [2] M. C. Weisskopf, B. Brinkman, C. Canizares, G. Garmire, S. Murray, L. P. Van Speybroeck: PASP **114**, 1 (2002). 360
- [3] F. Jansen, D. Lumb, B. Altieri, J. Clavel, M. Ehle, C. Erd, *et al.*: A&A **365**, 1 (2001). 360
- [4] R. Mewe: Atomic Physics of Hot Plasmas, in *X-Ray Spectroscopy in Astrophysics*, J. van Paradijs, J. A. M. Bleeker (Eds.) (Springer, Berlin 1999) p. 109. 361
- [5] D. A. Liedahl: Spectral Properties of PIE and NIE Plasmas, in *X-Ray Spectroscopy in Astrophysics*, J. van Paradijs, J. A. M. Bleeker (Eds.) (Springer, Berlin 1999) p. 189. 361
- [6] D. Porquet, J. Dubau: A&AS **143**, 495 (2000). 362, 363
- [7] T. R. Kallman, J. H. Krolik: XSTAR-A Spectral Analysis Tool, HEASARC NASA/GSFC, Greenbelt, MD (1995). 363
- [8] V. Decaux, P. Beiersdorfer, A. Ostereld, M. Chen, S. M. Kahn: ApJ **443**, 464 (1995). 366
- [9] S. S. Holt: in *High Resolution X-Ray Spectroscopy of Cosmic Plasmas*, P. Gorenstein, M. Zombeck (Eds.) (Cambridge University Press, Cambridge, 1990) p. 346. 366
- [10] F. Paerels: in *X-Ray Spectroscopy in Astrophysics*, J. van Paradijs, J. A. M. Bleeker (Eds.) (Springer, Berlin, 1999) p. 345 366
- [11] A. C. Brinkman, J. H. Dijkstra, W. F. P. A. L. Geerlings, F. A. van Rooijen, C. Timmerman, P. A. J. de Korte: ApOpt **19**, 1601 (1980). 367
- [12] F. D. Seward, *et al.*: ApOpt **21**, 2012 (1982). 367
- [13] T. H. Markert, C. R. Canizares, D. Dewey, M. McGuirk, C. S. Pak, M. L. Schattenburg: SPIE **2280**, 168 (1994). 368
- [14] A. C. Brinkman, T. Gunsing, J. S. Kaastra, R. van der Meer, R. Mewe, F. B. Paerels, *et al.*: SPIE **4012**, 81 (2000). 368

- [15] G. P. Garmire, M. W. Bautz, P. G. Ford, J. A. Nousek, G. R. Ricker: SPIE **4851**, 28 (1987). 368, 371
- [16] S. S. Murray, G. K. Austin, J. H. Chappell, J. J. Gomes, A. T. Kenter, R. P. Kraft, *et al.*: SPIE **4012**, 68 (2000). 368
- [17] J. W. den Herder, A. C. Brinkman, S. M. Kahn, G. Branduardi-Raymont, K. Thomsen, *et al.*: A&A **365**, L7-L17 (2001). 368
- [18] M. J. L. Turner, A. Abbey, M. Arnaud, M. Balasini, M. Barbera, *et al.*: A&A **365**, L27 (2001). 369, 371
- [19] K. Jahoda, J. H. Swank, A. B. Giles, M. J. Stark, T. Strohmayer, W. Zhang, E. H. Morgan: SPIE **2808**, 59 (1996). 369
- [20] Y. Tanaka, H. Inoue, S. S. Holt: PASJ **46**, L37 (1994). 371
- [21] L. Strueder, U. Briel, K. Dennerl, R. Hartmann, E. Kendziorra, N. Meidinger, *et al.*: A&A **365**, L18 (2001). 371
- [22] P. R. Roach and B. P. M. Helvenstein: Cryogenics **39**, 1015 (1999). 373
- [23] O. V. Lounasmaa: *Experimental principles and methods below 1K* (Academic Press, London, New York 1974). 373
- [24] A. T. Serlemitsos, M. SanSebastian, E. Kunes: Cryogenics **32**, 117 (1992). 373
- [25] A. E. Szymkowiak, R. L. Kelley, S. H. Moseley, C. K. Stahle: J. Low Temp. Phys. **93**, 281 (1993). 377
- [26] W. Cui, R. Almy, S. Deiker, D. McCammon, J. Morgenthaler, W. T. Sanders, R. L. Kelley, F. E. Marshall, S. H. Moseley, C. K. Stahl, A. E. Szymkowiak: SPIE **2280**, 362 (1994). 377
- [27] C. K. Stahle, C. A. Allen, K. R. Boyce, R. P. Brekosky, G. V. Brown, J. Cottam, E. Figueroa-Feliciano, M. Galeazzi, J. D. Gygas, M. B. Jacobson, R. L. Kelley, L. Dahai, D. McCammon, R. A. McClanahan, S. H. Moseley, F. S. Porter, L. E. Rocks, W. T. Sanders, C. M. Stahle, A. E. Szymkowiak, J. E. Vaillancourt: SPIE **4851**, 1394 (2003). 378, 390, 391
- [28] R. Fujimoto: personnel communication, NeXT Proposal Book (2003). 375
- [29] C. S. Bowyer, G. B. Field, J. E. Mack: Nature **217**, 32 (1968). 381
- [30] A. N. Bunner, P. L. Coleman, W. L. Kraushaar, D. McCammon, T. M. Palmieri: Nature **223**, 1222 (1969). 381
- [31] D. McCammon, D.N. Burrows, W. T. Sanders, W. L. Kraushaar: ApJ **269**, 107 (1983). 382
- [32] S. L. Snowden, R. Egger, M.J. Freyberg, D. McCammon, P. P. Plucinsky, W. T. Sanders, J.H.M.M. Schmitt, J. Trümper, W. Voges: ApJ **485**, 125 (1997). 382
- [33] D. McCammon and W. T. Sanders: Ann. Rev. Ast. Astrophs. **28**, 657 (1990). 382
- [34] D. McCammon, R. Almy, E. Apodaca, W. Bergmann Tiest, W. Cui, S. Deiker, M. Galeazzi, M. Juda, A. Lesser, T. Mihara, J. P. Morgenthaler, W. T. Sanders, J. Zhang, E. Figueroa-Feliciano, R. L. Kelley, S. H. Moseley, R. F. Mushotzky, F. S. Porter, C. K. Stahle, A. E. Szymkowiak: ApJ **576** 188 (2002). 382, 383, 384, 385
- [35] F. S. Porter, R. Almy, E. Apodaca, E. Figueroa-Feliciano, M. Galeazzi, R. Kelley, D. McCammon, C. K. Stahle, A. E. Szymkowiak, W. T. Sanders: Nucl. Inst. and Meth. A **444**, 175 (2000). 382
- [36] T. Kamae, H. Ezawa, Y. Fukazawa, H. Hirayama, E. Idesawa, N. Iyomoto, H. Kaneda, G. Kawaguti, M. Kokubun, H. Kubo, A. Kubota, K. Matsushita, K. Matsuzaki, K. Makishima, T. Mizuno, K. Nakazawa, S. Osone, H. Obayashi, Y.

- Saito, T. Tamura, M. Tanaka, M. Tashiro, J. Kataoka, T. Murakami, N. Ota, H. Ozawa, M. Sugizaki, K. Takizawa, T. Takahashi, K. Yamaoka, A. Yoshida, H. Ikeda, K. Tsukada, M. Nomachi: SPIE **314**, 2806 (1996). 386
- [37] S. I. Han, R. Almy, E. Apodaca, W. Bergmann, S. Deiker, A. Lesser, D. McCammon, K. Rawlins, R. L. Kelley, S. H. Moseley, F. S. Porter, C. K. Stahle, A. E. Szymkowiak: SPIE **3445**, 640 (1998). 390
- [38] R. L. Kelley, S. H. Moseley, C. K. Stahle, A. E. Szymkowiak, M. Juda, D. McCammon, J. Zhang: J. Low Temp. Phys. **93**, 225 (1993). 391
- [39] G. Hölzer, M. Fritsch, M. Deutsch, J. Härtwig, E. Förster: Phys. Rev. A **56**, 4554 (1997). 392
- [40] J. A. Chervenak, K. D. Irwin, E. N. Grossman, J. M. Martinis, C. D. Reintsema, M. E. Huber: Appl. Phys. Lett. **74**, 4043 (1999). 395
- [41] J. van der Kuur, P.A.J. de Korte, H. F. C. Hoevers, M. Kivirana, H. Seppä: Appl. Phys. Lett. **81**, 4467 (2002). 395
- [42] Rayleigh scattering, in: F. Salama (Ed.), NASA Lab. Astrophysics Workshop, Moffet Field, CA, 2002. 396
- [43] P. Beiersdorfer: Astron. Astrophys. Rev. **41**, 343 (2003). 396
- [44] M. LeGros, E. Silver, P. Beiersdorfer, J. R. C. López-Urrutia, K. Widmann, S. M. Kahn: Electron Beam Ion Trap Ann. Report, Lawrence Livermore National Laboratory, 1995, pp. 22–23, uCRL-ID-124429. 396
- [45] M. Laming, I. Kink, E. Takacs, J. V. Porto, J. D. Gillaspay, E. H. Silver, H. W. Schnopper, S. R. Bandler, N. S. Brickhouse, S. S. Murray, M. Barbera, A. k. Bhatia, G. A. Doschek, N. Madden, D. Landis, J. Beeman, E. E. Haller: ApJ **545**, L161 (2000). 396
- [46] E. Silver, H. Schnopper, S. Bandler, N. Brickhouse, S. Murray, N. Madden, D. Landis, J. Beeman, E. Haller, M. Barbera, G. Tucker, J. Gillaspay, E. Takacs, J. Porto, I. Kink: ApJ **541**, 495 (2000). 396
- [47] F. S. Porter, M. D. Audley, P. Beiersdorfer, K. R. Boyce, R. P. Brekosky, G. V. Brown, K. C. Gendreau, J. Gygas, S. M. Kahn, R. L. Kelley, C. K. Stahle, A. E. Szymkowiak: SPIE **4140**, 407 (2000). 396
- [48] F. S. Porter, P. Beiersdorfer, K. R. Boyce, G. V. Brown, H. Chen, R. L. Kelley, C. A. Kilbourne: Rev. Sci. Instr. **75**, 3772 (2204). 396
- [49] M. Levine, R. Marrs, D. Knapp, M. Schneider: Phys. Scr. **T22**, 157 (1988). 397
- [50] R. E. Marrs: Atomic, Molecular, and Optical Physics: charged particles, Vol. 29A of Experimental Methods in the Physical Sciences, Academic Press, Inc., San Diego, CA, 1995, chapter 14. Electron Beam Ion Traps. 397
- [51] P. Beiersdorfer, G. V. Brown, J. C. Lopez-Urritia, V. Decaux, S. R. Elliott, D. Savin, A. J. Smith, G. Stefanelli, K. Widman, K. L. Wong: Hyperfine Inter. **99**, 203 (1996). 397
- [52] D. W. Savin, B. Beck, P. Beiersdorfer, S. M. Kahn, G. V. Brown, M. F. Gu, D. A. Liedahl, J. H. Scofield: Phys. Scr. **T80**, 312 (1999). 399
- [53] P. Beiersdorfer: in *X-ray and Inner-Shell Processes*, T. A. Carlson, M. O. Krause, S. T. Manson (Eds.), (AIP, Knoxville, TN, 1990) p. 648. 399
- [54] M. D. Audley, R. Fujimoto, K. Mitsuda, K. Arnaud, K. C. Gendreau, K. R. Boyce, C. M. Fleetwood, R. L. Kelley, R. A. Keski-Kuhn, F. S. Porter, C. K. Stahle, A. E. Szymkowiak, J. L. Tveekrem, Y. Ishisaki, T. Mihara: in *Proceedings of a New Century of X-ray Astronomy*, H. Inoue and H. Kunieda (Eds.) (Astronomical Society of the Pacific, San Francisco, 2001), p. 516. 401

- [55] M. D. Audley, K. A. Arnaud, K. C. Gendreau, K. R. Boyce, C. M. Fleetwood, R. L. Kelley, R. A. Keski-Kuha, F. S. Porter, C. K. Stahle, A. E. Szymkowiak, J. L. Tveekrem, R. Fujimoto, K. Mitsuda, Y. Ishisaki, T. Mihara: SPIE **3765**, 729 (1999). 401
- [56] D. W. Savin, P. Beiersdorfer, S. M. Kahn, B. Beck, G. V. Brown, M. F. Gu, D. A. Liedahl, J. H. Scofield: Rev. Sci. Instr. **71**, 3362 (2000). 401
- [57] E. Träbert: Can. J. Phys. **80**, 1481 (2002). 401
- [58] E. K. Wahlin, J. S. Thompson, G. H. Dunn, R. A. Phaneuf, D. C. Gregory, A. C. H. Smith: Phys. Rev. Lett. **66**, 157 (1991). 401
- [59] D. W. Savin, S. M. Kahn, G. Gwinner, M. Grieser, R. Repnow, G. Saathoff, D. Schwalm, A. Wolf, A. Müller, S. Schippers, P. A. Závodszky, M. H. Chen, T. W. Gorczyca, O. Zatsarinny, M. F. Gu: ApJS. **147**, 421 (2003). 401
- [60] A. Chutjian: Phys. Rev. A **29**, 64 (1984). 401
- [61] G. V. Brown, P. Beiersdorfer, H. Chen, K. Scofield, K. R. Boyce, R. L. Kelley, C. A. Kilbourne, F. S. Porter, A. E. Szymkowiak, S. M. Kahn: Phys. Rev. Lett., submitted. 402, 403
- [62] K. Wong, P. Beiersdorfer, K. Reed, D. Vogel: Phys. Rev. A **51**, 1214 (1995). 402
- [63] S. Chantrenne, P. Beiersdorfer, R. Cauble, M. Schneider: Phys. Rev. Lett. **69**, 265 (1992). 402
- [64] R. Marrs, M. Levine, D. Knapp, J. Henderson: Phys. Rev. Lett. **60**, 1715 (1988). 402
- [65] H. Chen, P. Beiersdorfer, G. V. Brown, K. C. Gendreau, K. R. Boyce, R. L. Kelley, F. S. Porter, C. K. Stahle, A. E. Szymkowiak, S. M. Kahn, J. Scofield: ApJ **567**, L169 (2002). 402
- [66] H. Chen, P. Beiersdorfer, J. H. Scofield, G. V. Brown, K. R. Boyce, R. L. Kelley, C. A. Kilbourne, F. S. Porter, M. F. Gu, S. M. Kahn: ApJ **618**, 1086 (2005). 402
- [67] V. A. Krasnopolsky: Icarus **167**, 417 (2003). 403
- [68] H. R. Griem: in *Principles of Plasma Spectroscopy, 2nd Edition*, (Cambridge University Press, United Kingdom, 1997). 403
- [69] D. J. McComas, S. J. Bame, B. L. Barraclough, W. C. Feldman, H. Funsten, J. T. Gosling, P. Riley, R. Skoug: Geophys. Res. Lett. **25**, 1 (1998). 403
- [70] V. Kharchenko, A. Dalgarno: J. Geophys. Res. **105**, 18351 (2000). 403
- [71] V. Kharchenko, M. Rigazio, A. Dalgarno, V. A. Krasnopolsky: ApJ **585** L73 (2003). 403
- [72] J. B. Greenwood, I. D. Williams, S. J. Smith, A. Chutjian: ApJ **533**, L175 (2000). 404
- [73] J. B. Greenwood, A. Chutjian, S. J. Smith: ApJ **529**, 605 (2000). 404
- [74] V. A. Krasnopolsky: Icarus **128**, 368 (1997). 404
- [75] P. Beiersdorfer, L. Schweikhard, J. C. López-Urrutia, K. Widmann: Rev. Sci. Instr. **67**, 3818 (1996). 404
- [76] P. Beiersdorfer, C. M. Lisse, R. E. Olson, G. V. Brown, H. Chen: ApJ **549**, L147 (2001). 404
- [77] P. Beiersdorfer, R. E. Olson, G. V. Brown, H. Chen, C. L. Harris, P. A. Neill, L. Schweikhard, S. B. Utter, K. Widmann: Phys. Rev. Lett. **85**, 5090 (2000). 404

- [78] P. Beiersdorfer, K. R. Boyce, G. V. Brown, H. Chen, S. M. Kahn, R. L. Kelley, M. May, R. E. Olson, F. S. Porter, C. K. Stahle, W. A. Tillotson: *Science* **300**, 1558 (2003). 404, 405, 406
- [79] C. M. Lisse and D. J. Christian and K. Dennerl and K. J. Meech and R. Petre and H. A. Weaver and S. J. Wolk: *Science* **292**, 1343 (2000). 405
- [80] J. C. Cuillandre, G. A. Luppino, B. M. Starr, S. Isani: *SPIE* **4008**, 1010 (2000). 407
- [81] D. A. Harper, C. A. Allen, M. J. Amato, T. J. Ames, A. E. Bartels, S. C. Casey, R. J. Derro, R. Evans, I. Gatley, S. J. Heimsath, A. Hermida, M. Jhabvala, J. H. Kastner, R. F. Loewenstein, S. H. Moseley, R. J. Pernic, T. S. Rennick, H. E. Rhody, D. Sandford, R. A. Shafer, P. J. Shirron, G. M. Voellmer, S. Wang, J. Wirth: *SPIE*, **4014**, 43 (2000). 408
- [82] H. Kraus, F. von Feilitzsch, J. Jochum, R. L. Mössbauer, T. Peterreins, F. Pröbst: *Phys. Lett. B*, **231**, 195 (1989). 409
- [83] E. Figeroa-Feliciano: *Nucl. Inst. and Meth. A*, **520**, 496 (2004). 408, 409
- [84] K. D. Irwin, K. W. Lehnert: *Appl. Phys. Lett*, **85**, 2107 (2004). 410
- [85] P. K. Day, H. G. Leduc, B. A. Mazin, A. Vayonakis, J. Zmuidzinas: *Nature*, **425**, 817 (2003). 410
- [86] NASA/SEU 2003 Roadmap: *Beyond Einstein: From the Big Bang to Black Holes*, <http://universe.gsfc.nasa.gov/be/roadmap.html>. 411

Index

- ACIS, 368, 371, 405, 406
ADR, 373, 374, 376–379, 383, 384, 388, 389, 395, 400
Astro-E, 399
Astro-E2, 359, 360, 370, 372, 374, 376, 377, 381, 386–389, 393, 399, 405, 406
Beyond Einstein, 411
CCD, 359, 366, 368–372, 386, 405–407
CFH12K, 407
Chandra, 359, 360, 367–372, 388, 393, 405, 406
charge exchange, 381, 382, 401, 403–406
COBE, 374
comet, 386, 401, 403–406
Constellation-X, 359, 374, 376–381, 394, 408–411
cryo-cooler, 374, 376–379, 388, 389, 392, 395
deep implant, 386, 391
dielectronic recombination, 388
diffraction grating, 360, 366, 367
direct excitation, 362, 402
EBIT, 387, 388, 396–402, 404, 406
Einstein, 367
electron-impact excitation (EIE), 401, 402
EPIC, 369, 371, 372
EXOSAT, 367
field effect transistor (FET), 379, 408
Generation-X, 411
HETG, 368, 369, 372, 388
HgTe, 383, 390, 391
HXD, 386
LETG, 368
MAXIM, 411
Maxwellian distribution, 361, 399, 401
microcalorimeter, 360, 366, 372, 373, 378, 379, 382, 383, 387–390, 393, 395, 396, 399, 403, 408, 409, 411
multiplexer, 379, 395
NeXT, 359, 372, 375–377, 381, 394, 410
photoionization equilibrium (PIE), 361
Position Sensitive TES (PoST), 408, 409
proportional counters, 359, 360, 366, 369, 370, 381
radiative recombination, 361, 362, 366, 401–403
reflection grating, 367–369
RGS, 368, 369, 388
ROSAT, 382, 386, 403, 410
RXTE, 369
Super-EBIT, 398
superconducting quantum interference device (SQUID), 378, 379, 408, 410
TES, 373, 379, 395, 408, 409
transmission grating, 367, 368
X-ray absorber, 390, 391, 393, 408
X-ray absorber, 383, 391, 393, 409
XEUS, 359, 372, 376, 381, 394, 408, 410
XIS, 386

- XMM-Newton, 359, 360, 367–372, 388, 393
- XQC, 359, 374, 377, 381–386, 389–391, 393, 395, 400, 410
- XRS, 359, 360, 374, 376–381, 386–395, 408, 410
- XRS/EBIT, 396, 399–406